Rosette Trajectories Project

BIM 241 - Introduction to MRI

University of California, Davis
Department of Biomedical Engineering

Team members:

Linh Le

Valerie Porter

Janani Aiyer

Date submitted:
December 15th, 2020

Table of Contents:

Introduction: **2**

Methods: **2**

Results: **3**

Limitations/Discussions: **3**

Individual Explorations: **3**

I. Linh's Individual Exploration 4

Introduction: 4

Methods: 4

Results: (all figures are displayed in LL Appendix) 5

Discussion: 5

Further improvements: 6

II. Valerie's Individual Exploration 6

Introduction: 6

Methods: 6

Results: 7

Discussion: 9

Further improvements: 9

III. Janani's Individual Exploration 9

Introduction: 9

Methods: 10

Results: 11

Discussion: 11

Future Improvements: 12

Conclusion: **12**

Acknowledgement: **13**

References: **13**

Appendices: **14**

LL Appendix: 14

VP Appendix: 19

Equations: 19

Tables: 19

Figures: 22

JAA Appendix: 47

Figures: 47

Tables 53

Supplementary Material 54

Introduction:

Iron overload results from the body accumulating excess amounts of iron in the tissue, which can cause organ failure and death. MRI's T2* measurement is a clinically useful biomarker for iron quantification because of iron's paramagnetic properties that cause inhomogeneity and increase the local T2* measurement. T2* measurements of the heart and liver are the strongest prognostic markers of mortality for these patients.

However, there are many challenges that MRI faces with the iron assessment technique. T2* calculations are easily affected by motion artifacts. Motion artifacts leads to suboptimal calculations of T2*, particularly in the heart, which is a critically important organ to assess for iron accumulation. Thus, longer MRI scans with gating and breath holding techniques are currently used to help reduce these artifacts during scans. However these imaging techniques are limiting for pediatric and geriatric patients, as well as patients with motor control disorders. They require longer scan times, long breath holds and may even require sedation, which adds risk and expense for the patient. This indicates that there is a need for faster and safer MRI scanning techniques for iron accumulation assessment.

There are more robust methods for capturing images with motion than Cartesian, such as radial and spiral k-space sampling methods, such as rosette trajectories. Rosettes are flower-like k-space trajectories that utilize frequent sampling of the center of k-space to reduce noise and produce diffuse aliasing artifacts. Thus, this paper aims to improve the techniques for quantification iron overload via T2* MRI assessment by utilizing rosette trajectories to reduce motion artifacts during these scans.

Methods:

Imaging was performed on a GE Signa 450W MRi system with a 20-channel cardiac coil (GE Healthcare, Waukesha, WI) [1]. The imaging parameters used for Cartesian and Rosette are described in Table 1 from Bush [1]. There are 2 imaging datasets that are included in this study. There are 6 phantoms containing ferumoxytol. Cartesian and Rosette Multi Echo images were acquired for these phantoms in axial orientation. For vivo imagings, there are eight healthy volunteers and eighteen patients undergoing T_2* iron assessment. The reproducibility experiments were performed in breath hold scans, while the motion sensitivity experiments in were done by comparing free breathing and failed breath-hold T_2* scans from healthy subjects.

To determine the number of petals for rosette scans are defined as class II rosettes based on the improvement of the work of Noll [2] and Li et al [6].

$$\begin{aligned} &\textit{if } N \textit{ is odd},\ q = \{\tfrac{N+2}{N} + \tfrac{2(k-1)}{N},\ k \in Z^+\},\ \{Z^+\} \\ &\textit{if } N \textit{ is even},\ q = \{\tfrac{N+2}{N} + \tfrac{4(k-1)}{N},\ k \in Z^+\},\ \{Z^+\} \end{aligned} \tag{1}$$

where N is a number of petals demonstrated in the k-trajectories, k is an incrementing parameter, and q is a shape parameter defined as $\omega_2/\omega_1\ (\omega_1 >> \omega_2)$, where ω_1, ω_2 are rotational frequencies. As shown in Figure 1 from Bush et al., there are multiple echoes (i.e.

petals) in a single repetition with the trajectory sampling window centered at each k-space center crossing.

In order to constrain the sequence for elimination of eddy current and gradient timing-related artifacts, the maximum slew rate and the gradient amplitude are set as 75 mT/m/s and 40 mT/m, respectively. In this study, there were a total of 800 rotations performed, with 137.5 degrees for each repetition. A total readout duration was 16 msec with selected q at 2.2.

Results:

The obtained results are shown in Fig. 3 in Bush et. al. The heart and liver are visualized as the reconstructed image and the T_2* map respectively. The images were qualitatively scored from 1-5 by radiologists for the 3 techniques.

Rosette R2* (1/T2*) was linearly correlated with ferumoxytol concentration (r2 = 1.00) and not different from its corresponding Cartesian values (P = 0.16). During breath-holding, ungated rosette liver and heart T2* had lower spatial CoV and higher-qualitative scores (liver: 3.3 Cartesian, 4.7 rosette, heart: 3.0 Cartesian, 4.5 rosette, P = 0.005). During free-breathing and failed breath-holding, Cartesian images had average image quality with visible artifacts, on the other hand, rosette maintained good image quality, with minimal artifacts (P = 0.001).

Limitations/Discussions:

Rosette has comparable T_2* to Cartesian trajectories with high image quality, spatial resolution, reproducibility, low motion artifacts and reduced spatial variability to clinical procedure. The advantages over previous work is that there is no patient motion correction, it is ungated and has same scan times as the clinical standard.

Some limitations include the limited number of subjects, increased chance of gradient timing imperfections in Non-Cartesian sampling, the incorporation of motion directly into the reconstruction model and that Rosette T_2* maps are more sensitive to off-resonance artifacts than the typical cartesian maps.

Individual Explorations:

For our individual explorations, we aim to evaluate the effects of changing the number of petals and inclusion of off-resonant sources on the reconstructed images along with SNR calculations of Rosette, Cartesian and phantom data that was provided to us.

I. Linh's Individual Exploration

Introduction:

Quantitative T_2* MRI is clinically useful for diagnosing many diseases by determining tissue iron content. However, motion artifacts from patient's movements usually influence the results of estimating T_2*. In order to reduce the motion artifacts, people usually use breath holding as well as gating methods that eliminate respiratory and cardiac motion. However, these methods take longer scan time, and inefficient, which create more risk and are expensive. Therefore, rosette k-space trajectories were developed to reduce these risks and reduce motion artifacts for better quantification of T_2*.

In my experiment, the goal is to explore the trade-off of changing number of petals in rosette trajectories to motion artifacts and understand how it influences T_2* quantifications.

Methods:

I. Phantom imaging:

To assessing with the motion artifacts, the k-space data for a pulsing circle with diameter sinusoidally oscillating at input frequency was generated with the center at [0,0], starting time of diameter oscillation of 0.12 sec, frequency of oscillation of 1 Hz, amplitude of oscillation of 40, and the midpoint of diameter oscillation at 180. For this experiment, the maximum slew rate and maximum gradient amplitude were constrained 80 mT/m/ms and 40 mT/m, respectively. The total readout time per oscillation is 15 msec. The rotational angle is 137.5 degrees for each repetition. Echo time (TE) starts at 0.8 msec, with duration as 0.004 msec, and ends at 2.104 msec.

II. To determine the number of petals in the k-trajectories:

By applying the equation (1) described above, the number of petals was generated by changing the value of q with ω_1 is the oscillation frequency ($\omega_1 = 2\pi f$), and ω_2 is the revolution frequency ($\omega_2 = q \times \omega_1$), where f is the lowest frequency that reaches the hardware limitations. In this study, the experiment is done with different numbers of petals from 4 to 13 (Figure 2, 3 in LL Appendix) with corresponding q as shown in Table 1. To reduce the computational time, we ran the analysis with 80 rotations as shown in Figure 1.

III. Image reconstruction:

The images were constructed by a parallel imaging with the optimization equation as described in Equation (2) from Bush et al [1].

IV. Motion artifacts calculation:

To evaluate the motion artifacts at different numbers of petals, a localized motion-artifact metric is used in this experiment from Cheng et al [4]. Gradient entropy was recommended as a good metric for motion artifacts since it defines the image intensity gradient [4, 7]. In this experiment, the localized pixel of interest was selected at location of [256, 256] in phantom images. The gradient entropy metric (in mm) will be calculated based on the pixel of interest to estimate the motion.

V. T_2* Fitting:

T_2* relaxation refers to a decay of transverse magnetization (Mxy) and is one of the main determinants of image contrast. T_2* is always less than or equal T_2. Given the TE, T_2* was estimated from a measured T_2-weighted data (in our case, the phantom images). The signal is defined as:

$$S = A \times exp(-TE/T2) \quad (2)$$

Results: (all figures are displayed in LL Appendix)

The rosette trajectories with varying numbers of petals (i.e. numbers of echo times) produced results with different image reconstruction from phantom imagings as shown in Figure 4. The gradient amplitude increases from 27.41 mT/m to 29.86 mT/m as we increase the number of petals from 4 to 13 as shown in Table 1. It takes longer for the computational time to run at q=0.6 (i.e. 5 petals) with 2.82 seconds, and faster at q=0.27 (i.e. 11 petals) with 1.96 seconds. Motion artifacts changes are displayed in Figure 5, which shows that when we increase the number of petals, the motion artifacts corresponding to the pixel of interest will significantly reduce to around -0.2 mm. Figure 6 illustrates the T_2* fitting based on the given TE, and we have high T_2* values for 7 and 13 petals. Therefore, the optimal number of petals with low motion artifacts and better T_2* magnitude should be 7 or 13 petals. However, it takes more time to execute these models as shown in Table 1.

Discussion:

This study introduces the experiment of number of petals in Rosette trajectories to evaluate the trade-off between number of petals and motion artifacts. This shows that as we increase the number of petals, the motion artifacts tend to reduce, and the computational time is related to the value of q (i.e. higher q takes more time to run). However, there are still some fluctuated results in motion metric performance as shown in Figure 5. At 6 and 9 petals, there are more motion artifacts in the center of the image. This can be explained by the smaller values of q for 6 and 9 petals (i.e. the revolutionary frequency should be really smaller rather than the oscillation frequency). Another explanation is that there are not enough rotations to create a motion-robust image since we only experienced 80 rotations. Therefore, there are some limitations in this study. First, there are likely more factors that influence the motion artifacts, not only the number of petals. Since the value of q relates to the shape of the petals, and it shows in Table 1 and Figure 5 that there should be a relationship between q and motion artifacts metric. In addition, the number of rotations or repetitions should be another issue since we only experiment with 80 rotations. Moreover, the computational time is based on the MATLAB runtime, so for every loop that we calculated it might memorize the previous data, so the computational time might not be exactly accurate. Furthermore, the motion metrics are based on the gradient entropy from Cheng et al, but it is measuring the intensity at every pixel compared to the pixel of interest. However, we only experiment with only 1 pixel of interest, so we should extend this for other kernels. Finally, T_2* was quantified by fitting T_2 based on given phantom imaging only and there is a lack of actual Cartesian T_2* data to compare so it is hard to determine the accuracy of T_2* in this study.

Further improvements:

For future explorations, we should work more on calculating the time scan per petal, and investigate the trade-off with other factors, for example, number of rotations, different range of petals, and undersampling influences. For this experiment, we only work with phantom imaging, but we should extend this work with vivo imagings, and find a more sophisticated mapping algorithm for T_2* quantification.

II. Valerie's Individual Exploration

Introduction:

Signal-to-Noise-Ratio (SNR) is one of the common image quality measurements performed on images. Higher SNR intensities indicates how much more signal than noise is in the image. By having higher signal intensities (or lower noise) acquired, the image data will be more accurate. Because the rosette trajectories improved the image quality by reducing noise and motion artifacts, SNR comparisons were performed to determine how rosette trajectory *in vivo* images compared to traditional Cartesian images, and how rosette trajectories data was affected by different levels of noise and motion.

Methods:

I. *In Vivo* Cartesian and Rosette Data

The Rosette *in vivo* image data are from a breath held, ungated cardiac scan with short-axis slice prescription. The patient has liver iron but normal myocardial T_2*. There are 5 echo images and each image has 256 x 256 pixels at a resolution of 1mm and FOV of 25cm. The echo times ranged from 0.8 to 13.6 ms. See table 1 in Bush et. al paper[1] for the rest the parameter values.

The Cartesian image data are the clinical reference to the reference data. It is ECG/PPG gated cardiac scan. There are 8 echo images and each image has 256 x 256 pixels at a resolution of 1.5mm and FOV of 40cm. The echo times ranged from 1.1 to 10.2. See table 1 in Bush et. al paper[1] for the rest the parameter values for this data.

Both datasets only contain the real values of the intensities and were normalized to an intensity range of 0-255 values by finding the maximum value between both datasets and multiplying the data in both datasets by a factor of 255/(max value). (See Equation 1 in VP Appendix)

II. Dynamic LV Phantom Data

The dynamic left ventricle phantom image data is created with the rosette_test.m code. The phantom simulates a left ventricle by oscillating a ring with 250mm diameter as the heart wall and a ball in the center of the ring as the lumen with a 180mm diameter. The phantom is about double the size of a typical humans' heart, but this was to artificially decrease the FOV since we had problems changing the sampling of the k-space and k-trajectory data. This way

we could see in better detail how the phantom data is affected by adding noise and increasing oscillation.

The phantom data is 512 x 512 pixels with 12 echoes ranging from 1 to 3432 ms. These echo times seem long, but were given to us by the authors. The image intensity data is complex. To add noise to the dataset, I added these variables:

- noise2 = amp*randn([1 length(heart_data)]);
- amp = [0, 10^{-6}, 10^{-4}, 10^{-2}, 1, 10, 100];

where noise2 is the random gaussian noise, amp is the amplitude of the noise, and heart_data provides the size of the k-space dataset. The noise is then added to data, the k-space variable in the code.

To add noise, I multiplied each image pixel with a unique noise value found with noise2. To keep the random noise constant, I used the function rng(1) to maintain the same random noise and only changed the amplitude (amp).

To change the motion, I changed the variable ampl, which is the oscillation amplitude. The values I used for the oscillation amplitudes were [0, 20, 40, 60, 80, 100]. This amplitude is defined as 10mm x resolution in the code. Thus, the resolution is increasing as the motion increases.

III. SNR Calculations

For the *in vivo* data, I calculated the SNR with Equations 1-4 (see appendix) in a separate code script called VP_SNR_Code.m. Using ROIs and finding the mean standard deviation from all the ROIs has been shown to be a useful technique for calculating the noise in an image since the noise distribution should not change much across the image.[3] Thus, the mean of the standard deviation of ROI is a better approximation of the rician noise in the *in vivo* data.

For the phantom data, I calculated the SNR with equations 1, 2, and 5 (see appendix). The reason for using equation 5 is that since the code creates the phantom data without noise or without noise from motion, we can find the noise of noisy images by simply subtracting the no noise image from the noisy one. For the added noise experiment, the no noise image is the phantom image with no added noise. For the oscillation experiment, the no noise image is the phantom with an oscillation amplitude of zero.

Results:

1. *In vivo* Cartesian vs. Rosette data

The data for both of these graphs can be found in Table V1 and V2, and their images are in the figures section of the VP appendix.

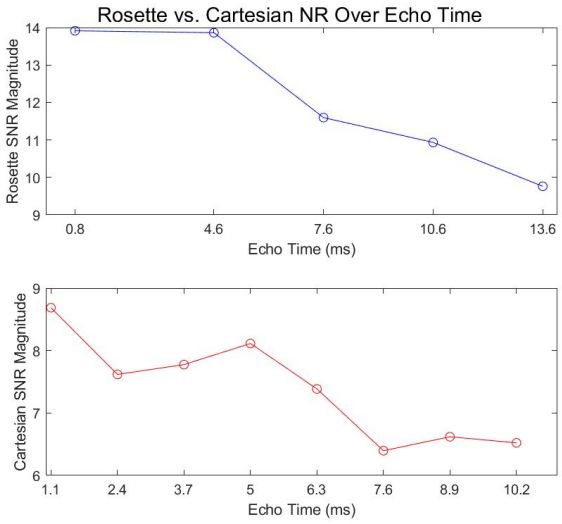

Figure V1: SNR magnitude over echo time for Rosette (top) and Cartesian (bottom) *in vivo* image data.

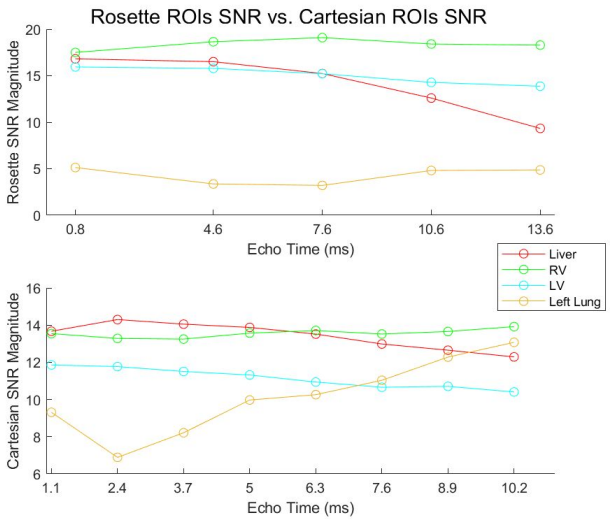

Figure V2: SNR magnitude of each ROI over echo time for Rosette (top) and Cartesian (bottom) *in vivo* image data.

2. Dynamic Phantom Data: a. Added Noise b. Varying Oscillation/Motion

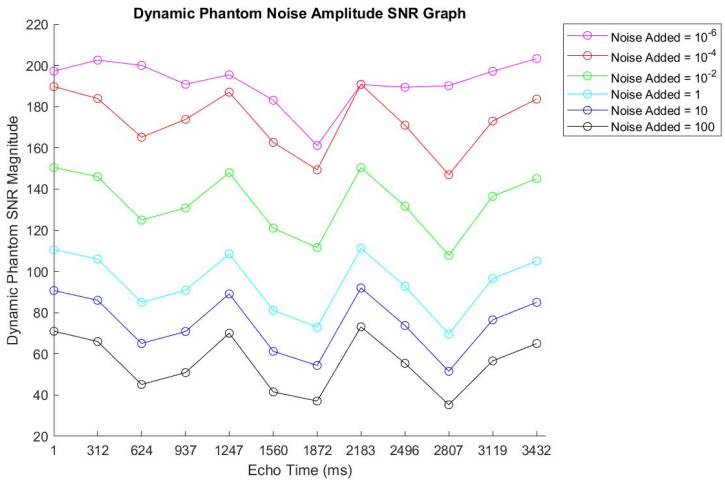

Figure V3: SNR Magnitude over time at each amplitude of added random gaussian noise.

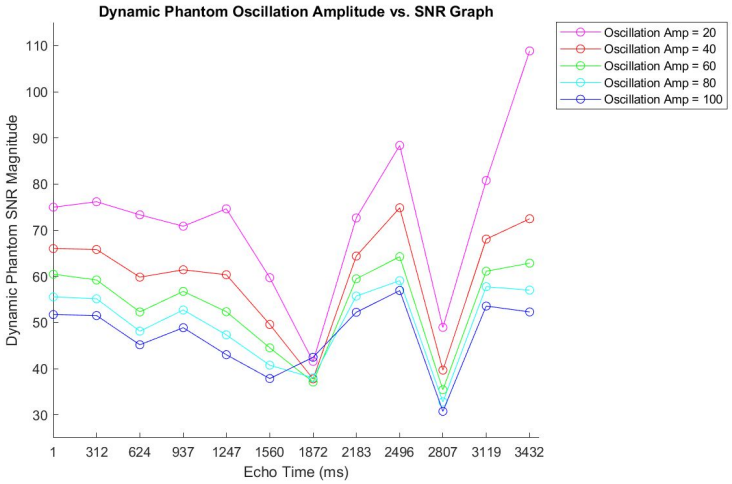

Figure V4: SNR Magnitude over time at each oscillation amplitude.

See Tables V3 and V4 for the data values of these graphs and their images in the VP Appendix.

Discussion:

The comparison between the rosette and cartesian image data shows that in both cases, the SNR tends decreases as echo time increases, which is to be expected due to signal decay. Overall, the SNR for the rosette data is higher than cartesian data including with the ROIs, except for the left lung. A direct comparison between the Cartesian and Rosette is not useful here due to the differences in FOV, echo times and resolutions which can drastically affect the SNR on its own. On the other hand, the SNR trends between the two methods for the ROI data show that the SNR values are more steady for the Rosette at every echo. Since the lungs have the least amount of signal compared to the other tissues, this steadiness indicates that the noise does not change much at each echo time for the Rosette, where it changes drastically depending on the echo time for the Cartesian method. Thus, the Rosette seems to limit changes in noise in images with motion artifacts.

For the phantom data, the graphs show that as the amplitude of the noise increases, the SNR values decrease for every echo image. The same is shown for increasing the oscillation amplitude. However, the change in noise amplitude seems to affect the Rosette method more strongly than changes in motion. This is likely because the amount of noise created from pure motion is smaller than the changes in noise amplitude that I used. Lastly, the changes in oscillation amplitude seem to not affect the SNR at the echo time of 1872ms, despite all the other echoes being affected by the change in amplitude. This may be due to the noise created by the motion of the phantom is not affecting the "tissue signals" that are being picked up at that echo time.

Further improvements:

For the in vivo data, the FOV and resolutions need to be fixed for a more comparable result. Furthermore, retaking the scans at the same echo times would further improve the SNR value comparison between the two methods.

For the dynamic phantom, the next step would be to see how the SNR is affected by added noise and motion together to see if there are any interesting trends at certain echo times, like at echo time 1872ms. Furthermore, it would be interesting to compare the SNR results of a static phantom to the dynamic phantom, to see how well the rosette method works on static MRI scan data.

III. Janani's Individual Exploration

Introduction:

Off-resonant (Off-Res) effects occur when the nuclear precession is out of phase or at a different frequency than the resonant frequency. The resultant dephasing contributes to a signal loss additional to intrinsic T2 dephasing. Off-Res sources may arise due to main field variations caused by magnetic design, susceptibility variations at a tissue-level or chemical shifts (eg. at 1.5T, there is a 220Hz off-resonance between fat and water).

Including the contribution of off-res sources, the receive signal equation becomes:

$$s(t) = \int_{x,y} m(x,y)\ e^{-2\pi i(k_x(t)x + k_y(t)y)} e^{-2\pi i \Delta f t} dxdy$$

With this exploration, I aim to explore the **potential effects of off-resonant sources on the final reconstructed image**.

Methods:

I. To generate the reconstructed images at off-res conditions, the following procedure was used:

1. The frequency at which the off-res images should be generated was identified (f=±1, ±16, ±64, ±128Hz)
2. The dynamic LV phantom portion was used, which read in generated data from the functions kspace_ball.m and kspace_dyn_circle.m
3. The time progression variable was identified as: t = TE0:dt:TE0+dt*(length(k(1, k_start:k_end)) - 1); where TE0 is excitation time, dt the k-space sampling rate and k_start, k_end represent the first and last k points
4. An element-wise multiplication was performed between the already generated on-res data and $e^{-2\pi i f t}$ (as per eqn above) and reconstructed using gridding reconstruction
5. The images are displayed for the 4th echo time = 937ms

II. To compare the generated off-res images with the reference/ ground truth on-resonance, the following procedure was used:

1. An ROI of size 140x190 was selected in the center region of the on and off-res images for comparison
2. The ROIs were passed through a function which calculated the image quality metrics between the predicted (off-res image ROI) and actual (on-res image ROI) images
3. Image quality metrics were used in accordance with metrics used in *[5]*
4. Quantitative metrics used are MSE, PSNR, R^2 Value, RMSE, NRMSE, MAPE and SSIM. The metrics and their practical application are described in detail in *JAA Appendix, Supplementary Material, pg. 54*

III. To provide a conclusive result between Linh's, Valerie and my work, the SNRs of on and off-res images with different numbers of petals were calculated as follows:

1. To incorporate a change in the number of petals, the shaping factor (q) was varied
2. The number of petals was changed between 5, 7 and 13 petals. 11 petals are the original number of petals, so it was not considered in this section of the study. Results for 11 petals are shown in *Results, Section I.*
3. Off-res images were generated as described in *Methods, Section I* at constant 64Hz
4. Using Valerie's SNR method of adding Rician noise, the SNRs were calculated

Results:

I. **Off-Res at Diff Freq:** ***Refer Fig. 1 A-P in JAA Appendix, pg. 47-50***

II. **Quantitative Metrics:** ***Refer Table 1 in JAA Appendix, pg. 53***

III. **Effect of Changing No. of Petals on SNR of Off-Res Images:** ***Refer Fig. 2 A-F, pg. 51-52 and Table 2, pg. 54 in JAA Appendix***

The lowest MSE, RMSE, NRMSE AND MAPE are obtained when the off-res F = ±1Hz with values **0.032, 0.178, 0.098 and 11.3** respectively. The highest values of these metrics are at ±128Hz with values **0.83, 0.911, 0.5 and 44.019** respectively. The highest values of R^2 , PSNR and SSIM are calculated for a F= ±1Hz at **0.983, 63.127 and 0.491** respectively. The corresponding lowest values are at 128Hz with **0.579, 48.943 and 0.166** respectively.

The highest SNR value of **202.54 for on-res and 201.08 for off-res** is obtained for 7 petals with a constant F = 64Hz. The lowest SNR is for 5 petals at **175.01 for on-res and 179.05 for off-res**. The figures obtained show good correlation with the obtained SNR results.

Discussion:

I. Off-Resonance Image Generation

The reconstructed images were generated for ±(1, 16, 64, 128Hz). The negative frequency reconstructions did not show any visible difference from their positive frequency counterparts. The results for the positive and negative frequencies can be found in the *Appendix Section, Fig. 1 (A-P), pg. 50-51*

The reconstructed image with off-res sources at 1Hz seems quite like the original, with no visible differences. At 16Hz, we start to see a drop in image quality. The inner and outer circle do not have a clear barrier of distinction like the black ring visible in the normal image, however, there is still some degree of visibility of the two circles. The image at 64Hz is significantly different from the on-res image in that there is no distinction between the two circles, except for the difference in color. This could be due to aliasing in the off-res image. At 128Hz, the reconstructed image is completely different from the on-res image and the outer circle is nearly completely aliased.

The dynamic phantom is constructed such that it can mimic the Left Ventricle, which implies that the inner and outer circle have different T2 values. From the off-res images, it is safe to say that the T2 of the inner circle (resembling blood) is higher than that of the outer circle (resembling heart tissue), which holds true when compared with biological T2 values. The inner circle seems to show lower signal decay, implying a higher T2 value. However, the outer circle in comparison shows a quick signal decay with the inclusion of off-res sources, implying a lower T2 time.

II. Quantitative Metrics

Consistent with the findings in *Results Section I.*, the best performing image, F=1Hz has the highest PSNR, R^2 Value and SSIM with the lowest MSE, RMSE, NRMSE and MAPE. The image that was visually the most different from the on-res image at F = 128Hz has the lowest PSNR, R^2 Value and SSIM with the highest MSE, RMSE, NRMSE and MAPE. The Quantitative Metrics for the frequencies and their corresponding negative values are quite similar, this is probably because there is no visible difference in their image quality.

The metrics gradually regressed with an increase in the frequency value. However, it is difficult to come to a rigid conclusion about the relationship between the frequency and the corresponding reconstructed image quality. In the frequencies considered, the image quality decreases with an increase in the |off-res frequency|.

III. Effect of Changing Number of Petals on the SNR of Off-Resonance Images

Using a constant frequency of 64Hz, the off-res image generated for a k-space sampling trajectory with 7 petals seems to be most similar to the on-res image. This is because of a clearer contrast between the inner and outer circle than for the 5 and 13 petal trajectories. This is consistent with the results obtained in *Results*, *Table 2, pg. 54*. The SNR for 7 petals is the highest and the SNR for 5 petals is predictably the lowest. The on-res image is independent of the off-res frequency. This was true for previous sections as well, but is confirmed after a comparison of the on-res images generated in *mine and Linh's study*.

Future Improvements:

Work on using different types of phantoms over a larger range of frequency values, identify better metrics for image quality evaluation, evaluate motion effects of the dynamic phantom and explore the degree of sensitivity of non-cartesian trajectories to off-res sources compared to their cartesian counterparts.

Conclusion:

Increasing the number of petals leads to a decrease in motion artifacts, with optimal performance at 7 or 13 petals. There are some limitations in our study such as the assumption of same petal shape, number of rotations, and scan time in the analysis.

For the *in vivo* data, the Rosette method has higher SNR values than the Cartesian method, but have different values for their FOVs, resolutions, and echo times. The ROI SNR trends did show that noise is more constant in the Rosette images and shows that the Rosette is not as affected by the noise caused by the motion artifacts from the heart. The phantom experiments showed that random gaussian noise affects SNR more than the motion. At the echo

time 1872ms, the motion did not seem to change the SNR at all. Thus, the motion may not be affecting the signal from the tissues that are detected at that echo time.

For the frequency range considered, there was an overall improvement in quality, with a decrease in frequency. This was proven visually and through the image quality metrics of MSE, PSNR, R-Squared, RMSE, NRMSE, MAPE and SSIM. The relationship between changing number of petals on the SNRs of on and off-res images was also considered and 7 petals was found to have the best performance, with the highest SNR.

Acknowledgement:

The Rosette Team is thankful for the help, support and encouragement from our BIM241 instructor Dr. Audrey Fan and our TA, Greg Wheeler. We are also grateful to the authors of the reference paper [1], Dr. Adam Bush and Dr. Shreya Ramachandran for providing us with code, data and constructive advice throughout the course of the project.

References:

1. Bush, A.M., Sandino, C.M., Ramachandran, S., Ong, F., Dwork, N., Zucker, E.J., Syed, A.B., Pauly, J.M., Alley, M.T. and Vasanawala, S.S. (2020), Rosette Trajectories Enable Ungated, Motion‐Robust, Simultaneous Cardiac and Liver T2* Iron Assessment. J Magn Reson Imaging, 52: 1688-1698. https://doi.org/10.1002/jmri.27196
2. D. C. Noll, "Multishot rosette trajectories for spectrally selective MR imaging," in IEEE Transactions on Medical Imaging, vol. 16, no. 4, pp. 372-377, Aug. 1997, doi: 10.1109/42.611345.
3. “MR Quality Control: SNR - How do you measure signal-to-noise in an image?” Questions and Answers in MRI. http://mriquestions.com/signal-to-noise.html. Accessed 1, Dec. 2020.
4. Cheng JY, Alley MT, Cunningham CH, Vasanawala SS, Pauly JM, Lustig M. Nonrigid motion correction in 3D using autofocusing with localized linear translations. Magn Reson Med. 2012 Dec;68(6):1785-97. doi: 10.1002/mrm.24189. Epub 2012 Feb 3. PMID: 22307933; PMCID: PMC3376676.
5. Zeng DY, Shaikh J, Holmes S, et al. Deep residual network for off resonance artifact correction with application to pediatric body MRA with 3D cones. Magn Reson Med 2019;82:1398-1411.
6. Li Y, Yang R, Zhang C, Zhang J, Jia S, Zhou Z. Analysis of generalized rosette trajectory for compressed sensing MRI. Med Phys. 2015 Sep;42(9):5530-44. doi: 10.1118/1.4928152. PMID: 26329000.
7. McGee KP, Manduca A, Felmlee JP, Riederer SJ, Ehman RL. Image metric-based correction (autocorrection) of motion effects: analysis of image metrics. J Magn Reson Imaging. 2000 Feb;11(2):174-81.

Appendices:

LL Appendix:

Number of petals	q	Gradient amplitude (mT/m)	Computational Time (s)
4	0.5000	27.41	2.33
5	0.6000	26.28	2.82
6	0.6667	25.50	2.41
7	0.4286	28.17	2.52
8	0.7500	24.52	2.42
9	0.5556	26.79	1.95
10	0.4000	28.46	2.26
11	0.2727	29.57	1.96
13	0.2308	29.86	2.03

Table 1. Corresponding gradient amplitude (mT/m), computational time, and q values corresponding to generated number of petals from k-trajectories.

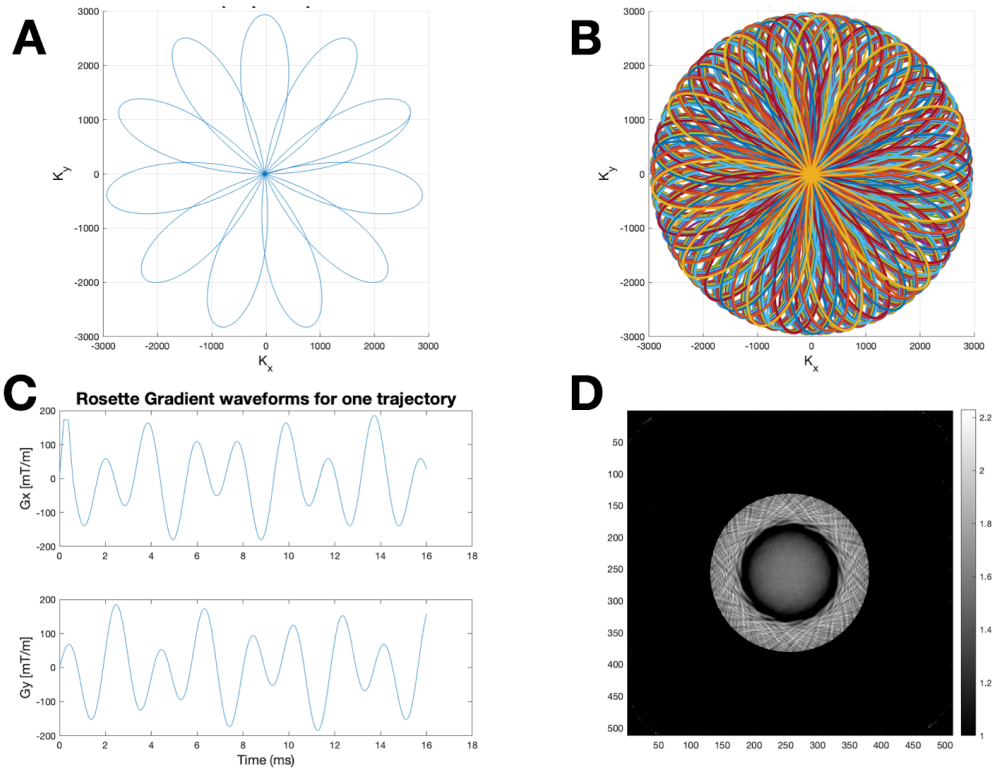

Figure 1. (A) Single rosette repetition at q = 0.27, with each petal corresponding to the effective echo time . (B) Rotating the rosette repetition by the golden angle (137.5 degree) in k space. (C) The corresponding readout gradient and spoiling gradient waveforms are shown. (D) The image reconstruct

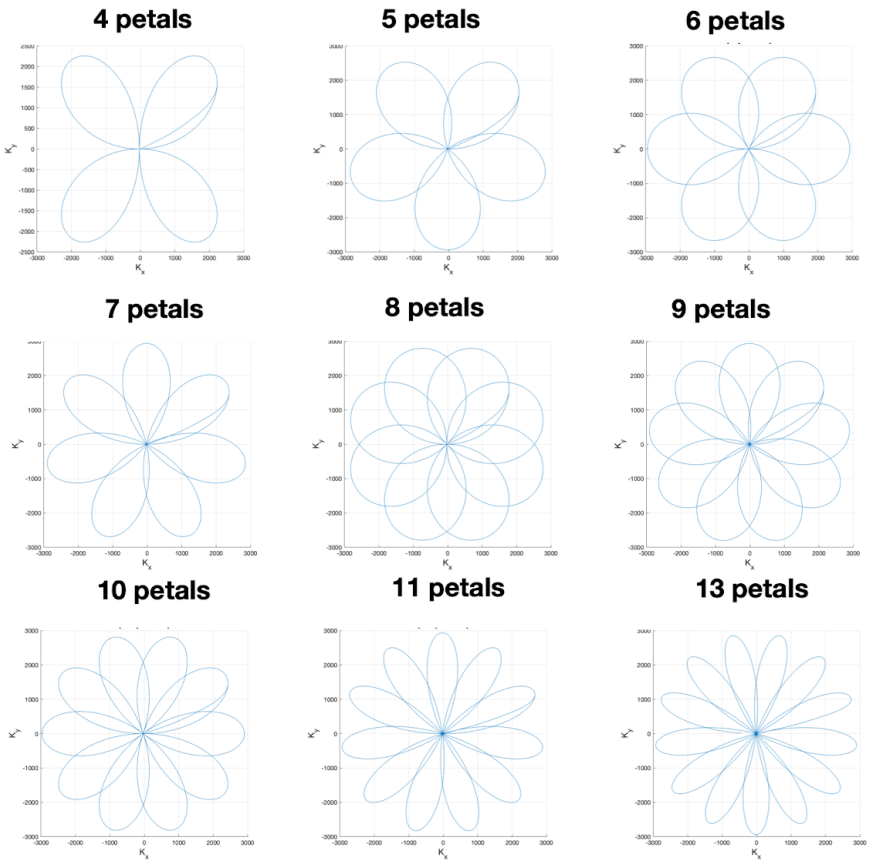

Figure 2. Single repetitions with varying q values to create 4 to 13 petals based on Table 1.

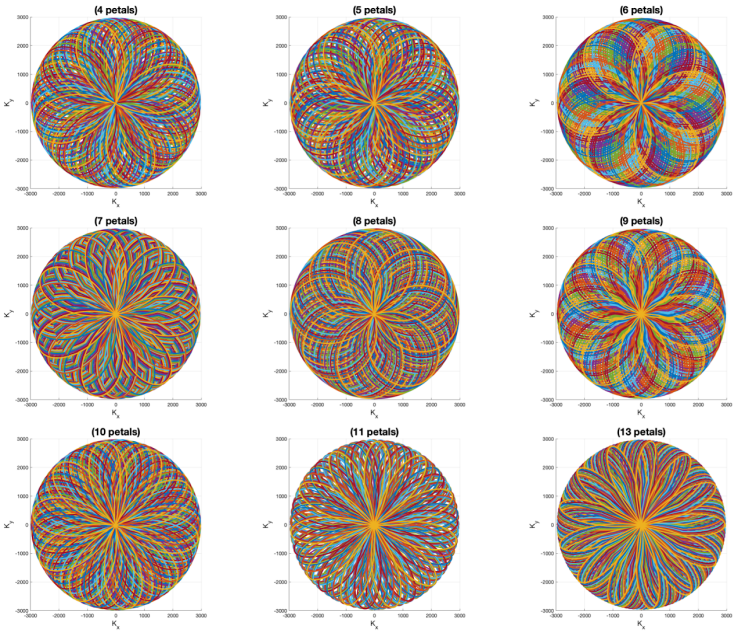

Figure 3. Rotating 80 times for the rosette repetition by golden angle (137.5 degree) in k-space

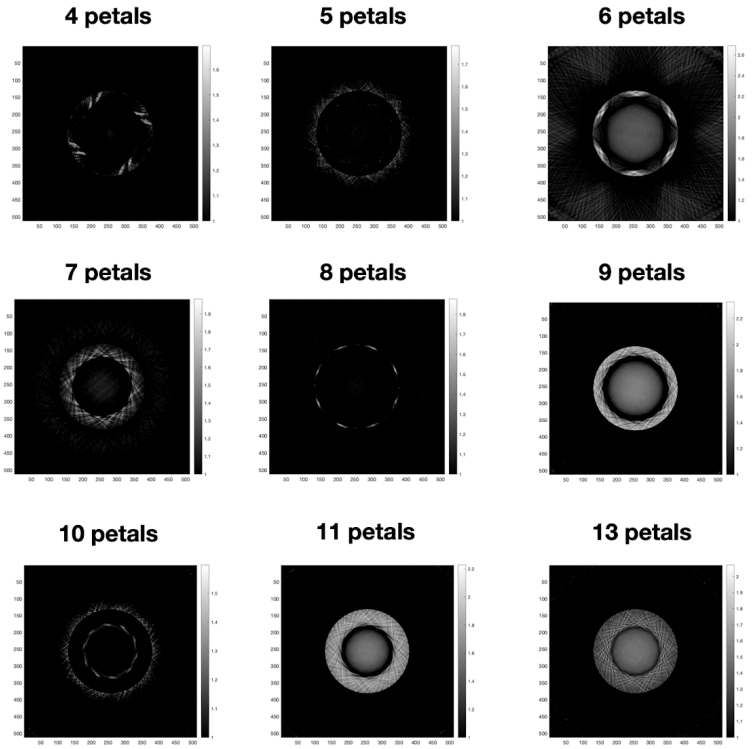

Figure 4. Reconstructed phantom images for varying Rosette trajectories from 4 to 13 petals. The motion-induced aliasing artifacts in individual images are reduced as the increasing number of petals. Higher number of petals in rosette reconstruction also produce better image quality.

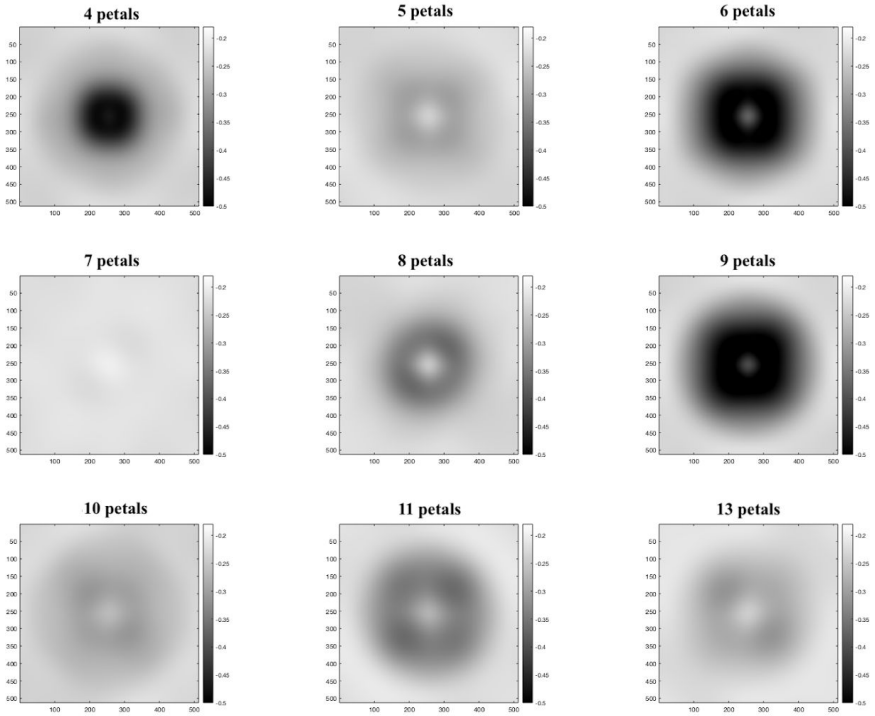

Figure 5. A motion metric maps (in grayscale) from phantom images for individual models of petals at every pixel compared to the pixel of interest (i.e. [256 256]). The lower the value of motion metrics (close to light color) means the intensity of motion is less, and vice versa. The scale for this motion metric is from -0.5 to -0.2 (mm)

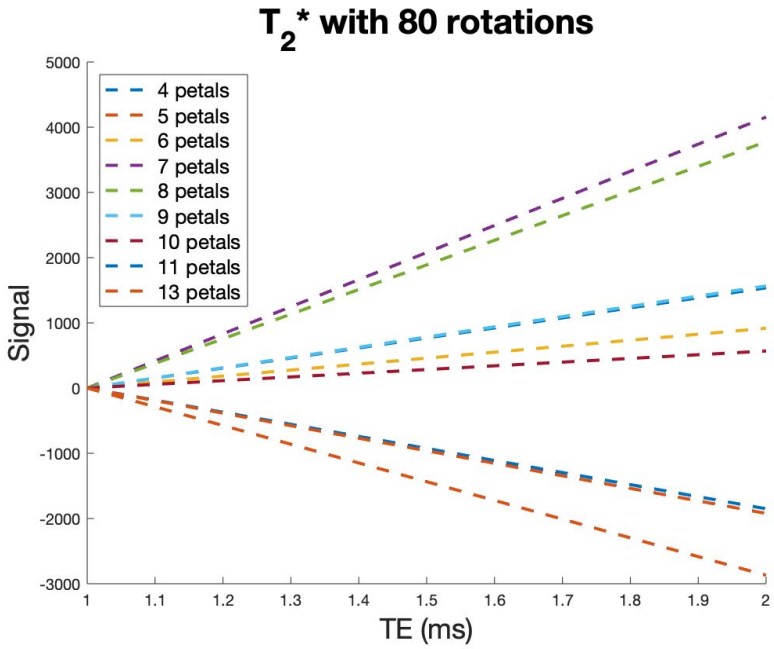

Figure 6. T2* fitting based on the give TE (from 0.8 to 2.1 msec), and the phantom imagings. The absolute value of average magnitude of T2* for 7 petals and 13 petals are higher than other petal-models.

VP Appendix:

Equations:

Equations V1: $$SNR = 20 * log_{10}(\frac{signal}{noise})$$

Equation V2: $$signal = mean(entire\ image)$$

Equation V3: $$noise = mean(noise\ of\ each\ ROIs)$$

Equation V4: $$noise\ of\ each\ ROI = std(image\ of\ ROIs)$$

Equation V5: $$noise = mean(image\ with\ noise - image\ no\ noise)$$

Tables:

Table V1: Rosette SNR Data						
Echo Times	**0.8 (ms)**	**4.6 (ms)**	**7.6 (ms)**	**10.6(ms)**	**13.6(ms)**	**AVG**
Total SNR	13.9135	13.8624	11.5956	10.9339	9.7628	12.0136
Liver SNR	16.8151	16.5124	15.2369	12.5997	9.3344	14.0997
RV SNR	17.5079	18.6562	19.0962	18.4146	18.2887	18.3927
LV SNR	15.9452	15.7880	15.2225	14.2843	13.8737	15.0228
Left_Lung SNR	5.1272	3.3643	3.2064	4.8104	4.8683	4.2753

Table V2: Cartesian SNR Data									
Echo Times:	**1.1 (ms)**	**2.4 (ms)**	**3.7 (ms)**	**5.0 (ms)**	**6.3 (ms)**	**7.6 (ms)**	**8.9 (ms)**	**10.2 (ms)**	**AVG**
Total SNR:	8.6864	7.6178	7.7750	8.1132	7.3846	6.3957	6.6193	6.5216	7.3892
Liver SNR:	13.6704	14.2988	14.0513	13.8749	13.5179	12.9843	12.6509	12.2898	13.4173
RV SNR:	13.5439	13.2837	13.2500	13.5686	13.7088	13.5215	13.6560	13.9183	13.5563
LV SNR:	11.8558	11.7687	11.5072	11.3177	10.9373	10.6589	10.7057	10.4050	11.1445
Left_Lung SNR:	9.3118	6.8869	8.2107	9.9716	10.2592	11.0329	12.2805	13.0740	10.1284

Table V3: Dynamic Phantom with Added Noise SNR Magnitude Values						
	Noise Amplitudes of Random Gaussian Noise:					
Echo Times	**10^{-6}**	**10^{-4}**	**10^{-2}**	**1**	**10**	**100**
1 (ms)	197.2607	189.7259	150.4641	110.6149	90.7589	70.9841
312 (ms)	202.6161	183.9365	145.9964	106.0010	86.0021	66.0076
624 (ms)	200.0224	165.1538	124.9665	85.0212	65.0549	45.1483
937 (ms)	190.8451	173.8043	130.8555	90.8621	70.8733	50.9111
1247 (ms)	195.4619	186.9928	147.9145	108.5512	89.1252	70.0203
1560 (ms)	183.1131	162.6682	120.9891	81.1041	61.2377	41.5241
1872 (ms)	161.1301	149.3118	111.5950	72.9566	54.3835	37.0971
2183 (ms)	190.7353	190.8219	150.4075	111.2681	92.0047	73.1355
2496 (ms)	189.4196	170.9740	131.6711	92.7610	73.7474	55.4106
2807 (ms)	190.1660	146.9496	107.8156	69.6339	51.5471	35.2794
3119 (ms)	197.1843	173.0081	136.5092	96.5180	76.5328	56.5666
3432 (ms)	203.2994	183.6614	145.0262	105.0259	85.0268	65.0315

Table V4: Dynamic Phantom with Varying Oscillation SNR Magnitude Values					
	Oscillation Amplitude:				
Echo Times	**20**	**40**	**60**	**80**	**100**
1 (ms)	74.9773	66.0065	60.4607	55.5426	51.7070
312 (ms)	76.1556	65.8260	59.2134	55.1448	51.5079
624 (ms)	73.3277	59.8176	52.2918	48.1067	45.1668
937 (ms)	70.8561	61.4141	56.7373	52.7111	48.8627
1247 (ms)	74.6303	60.3457	52.3356	47.3132	43.0150
1560 (ms)	59.7054	49.5673	44.5107	40.7365	37.8478
1872 (ms)	41.5608	37.7591	37.0832	38.0086	42.4625
2183 (ms)	72.6623	64.3823	59.4552	55.7165	52.2100
2496 (ms)	88.3597	74.8503	64.2499	59.0639	56.9232
2807 (ms)	48.9326	39.6825	35.4191	32.7930	30.7437
3119 (ms)	80.7742	68.0624	61.0993	57.7447	53.5622
3432 (ms)	108.8401	72.4648	62.8460	57.0014	52.2874

Figures:

Figure V5:

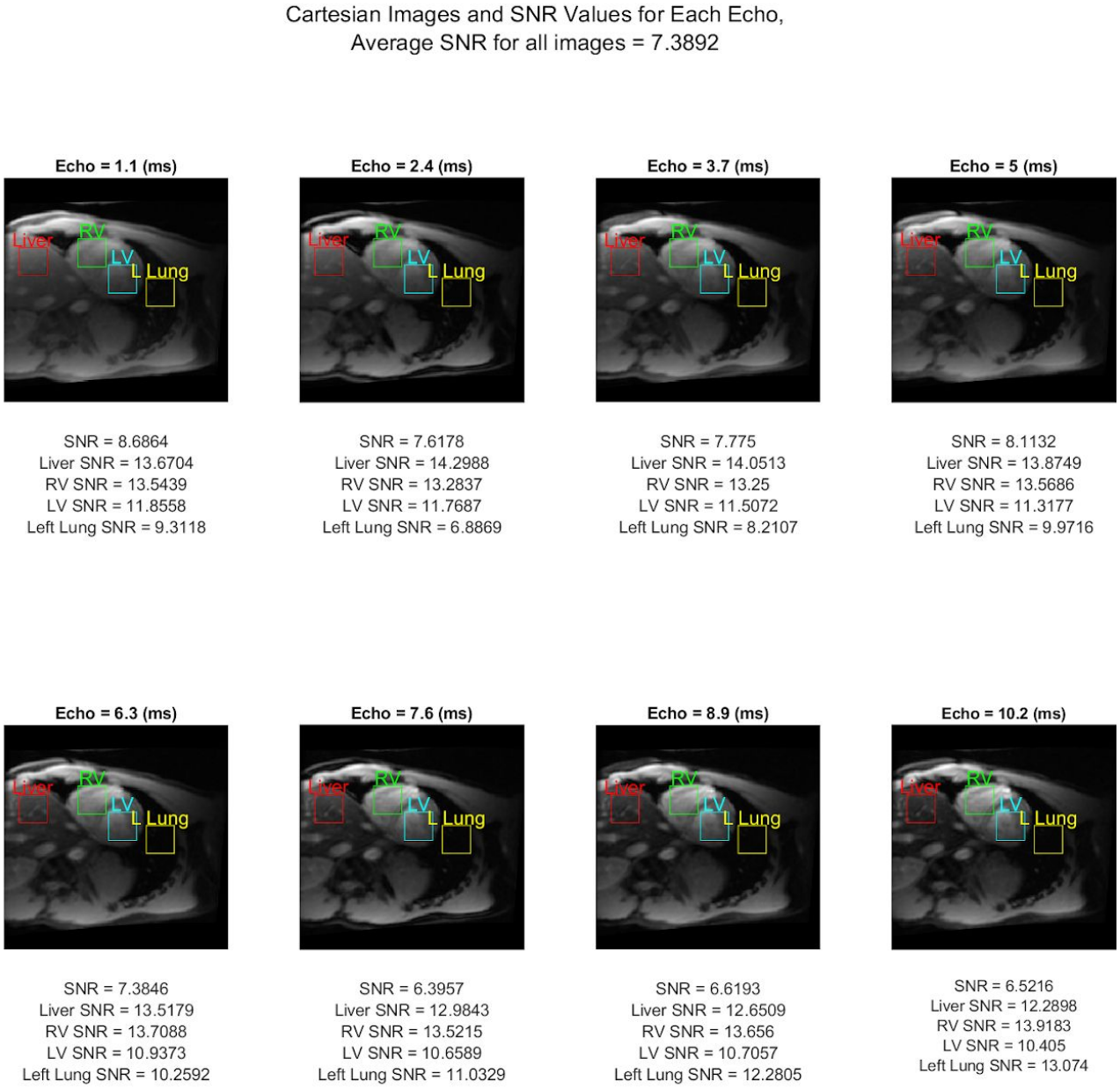

Figure V6:

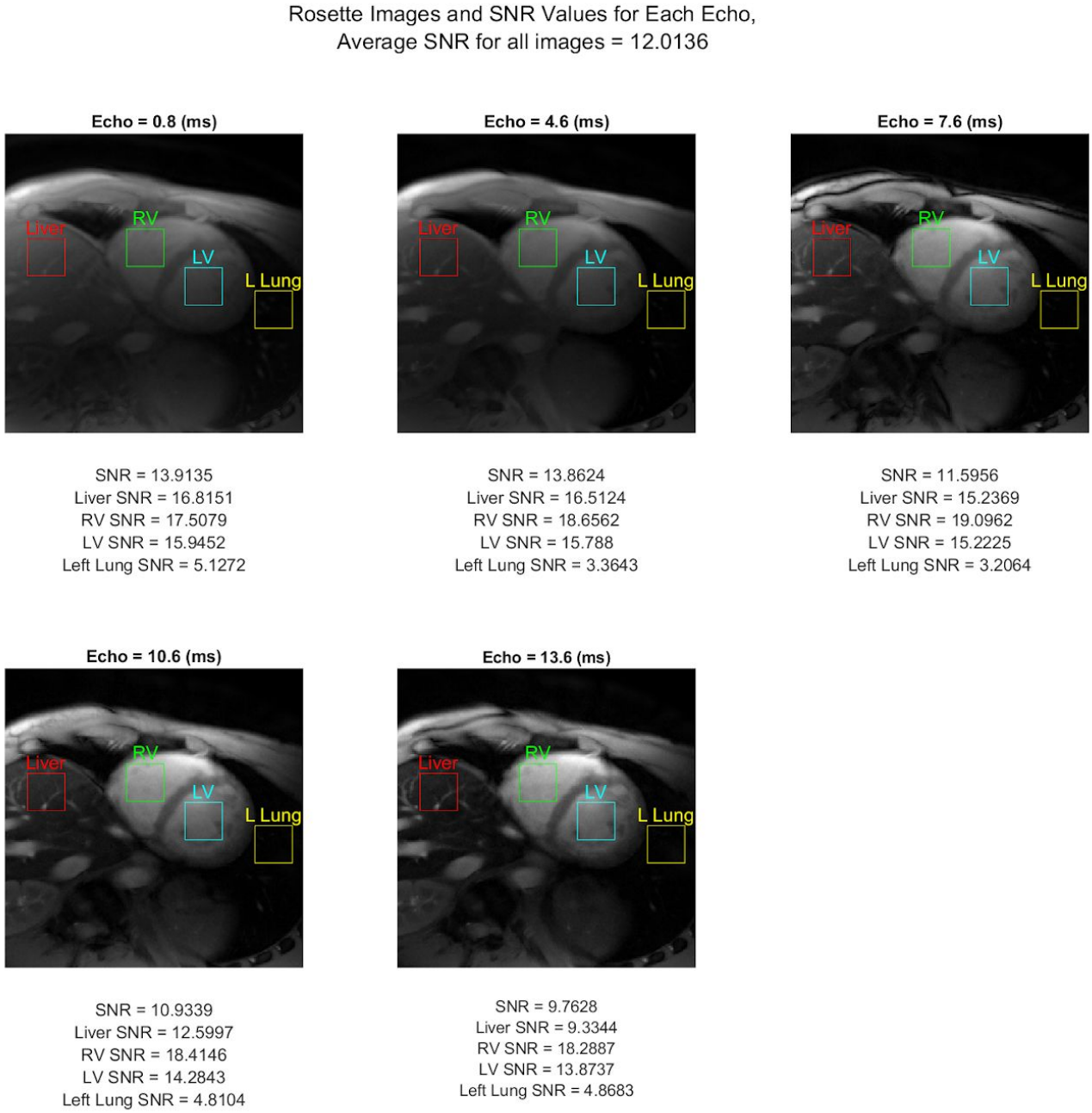
Rosette Images and SNR Values for Each Echo,
Average SNR for all images = 12.0136
Echo = 0.8 (ms)
Liver
RV
LV
L Lung
SNR = 13.9135
Liver SNR = 16.8151
RV SNR = 17.5079
LV SNR = 15.9452
Left Lung SNR = 5.1272
Echo = 4.6 (ms)
Liver
RV
LV
L Lung
SNR = 13.8624
Liver SNR = 16.5124
RV SNR = 18.6562
LV SNR = 15.788
Left Lung SNR = 3.3643
Echo = 7.6 (ms)
Liver
RV
LV
L Lung
SNR = 11.5956
Liver SNR = 15.2369
RV SNR = 19.0962
LV SNR = 15.2225
Left Lung SNR = 3.2064
Echo = 10.6 (ms)
Liver
RV
LV
L Lung
SNR = 10.9339
Liver SNR = 12.5997
RV SNR = 18.4146
LV SNR = 14.2843
Left Lung SNR = 4.8104
Echo = 13.6 (ms)
Liver
RV
LV
L Lung
SNR = 9.7628
Liver SNR = 9.3344
RV SNR = 18.2887
LV SNR = 13.8737
Left Lung SNR = 4.8683

Dynamic Phantom (Noise Added) Images from SNR Calculation:

Figure V7 and V8:

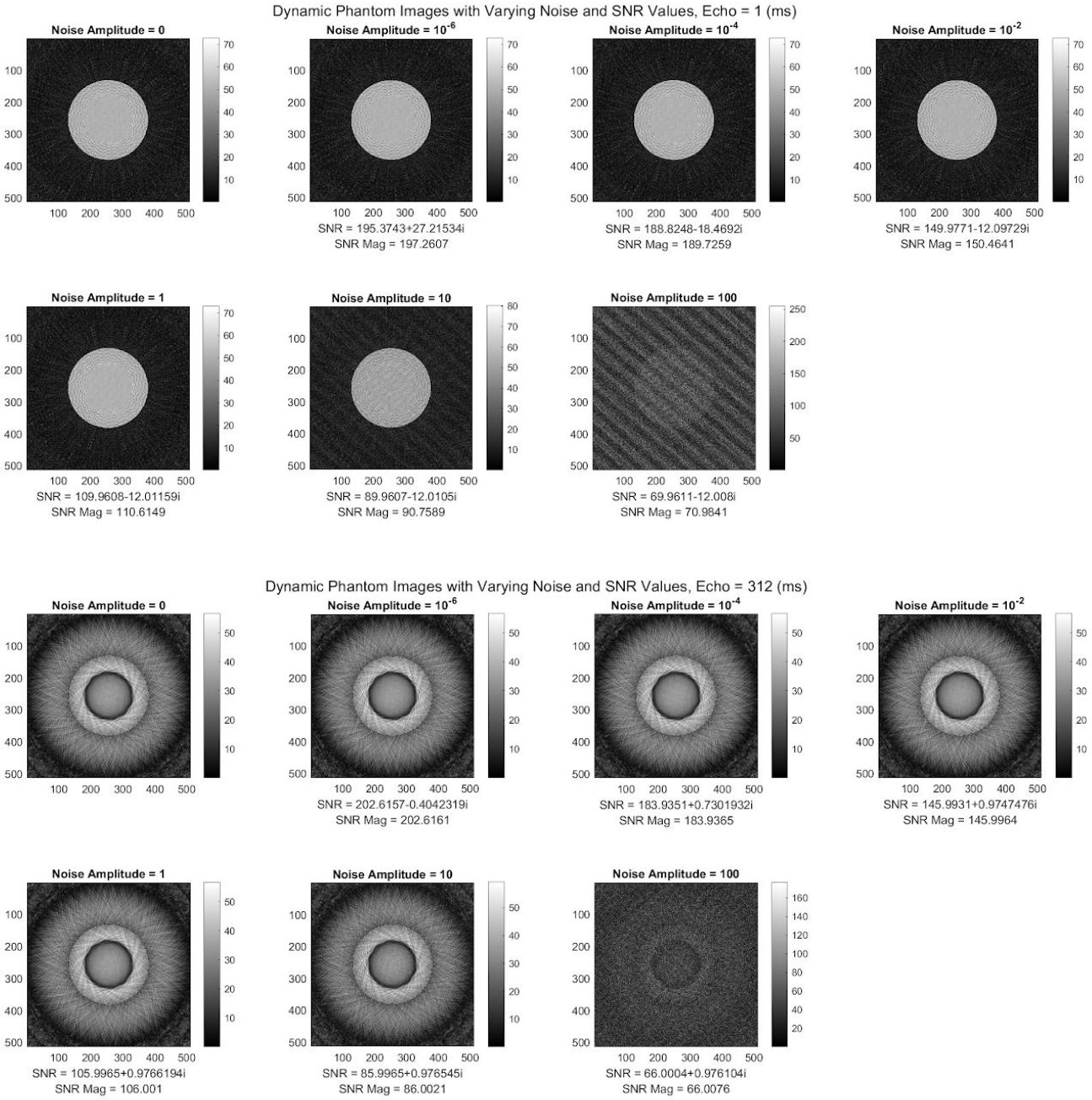

Figure V9 and V10:

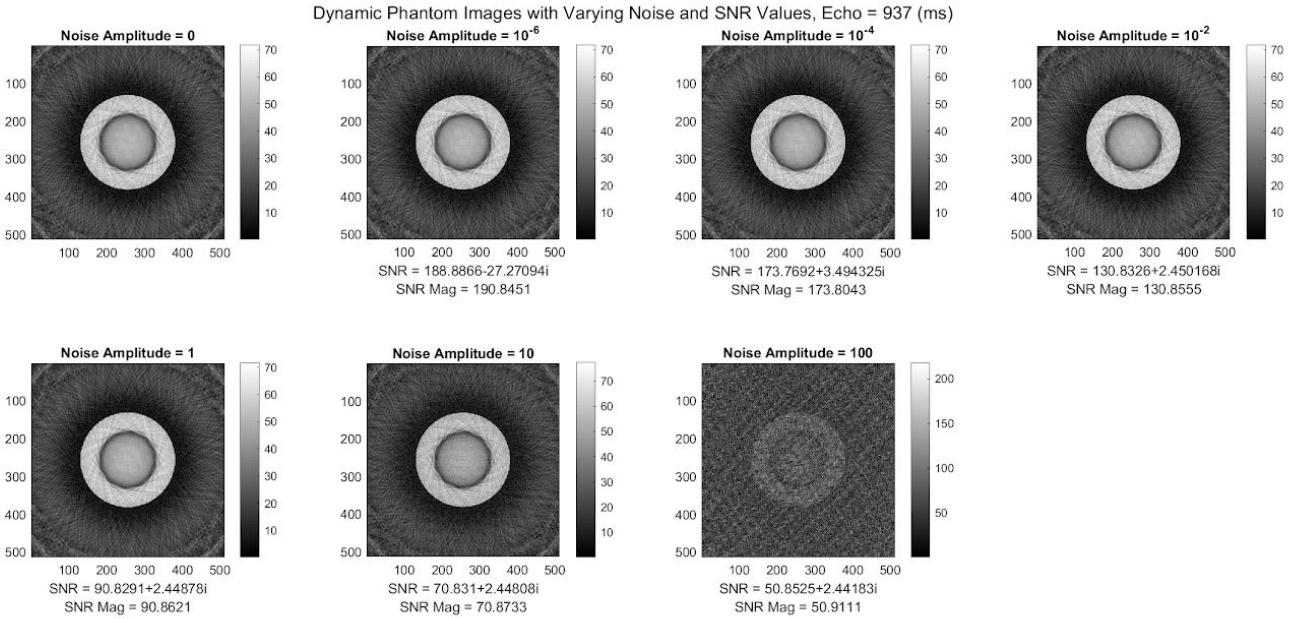

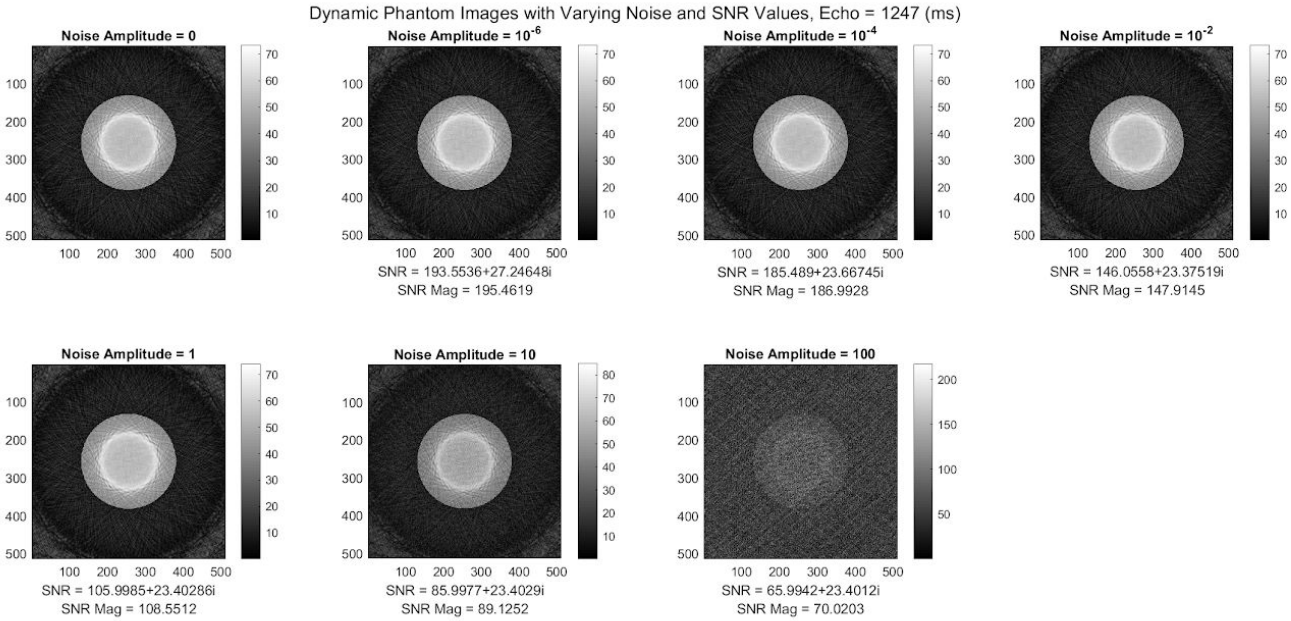

Figure V11 and V12:

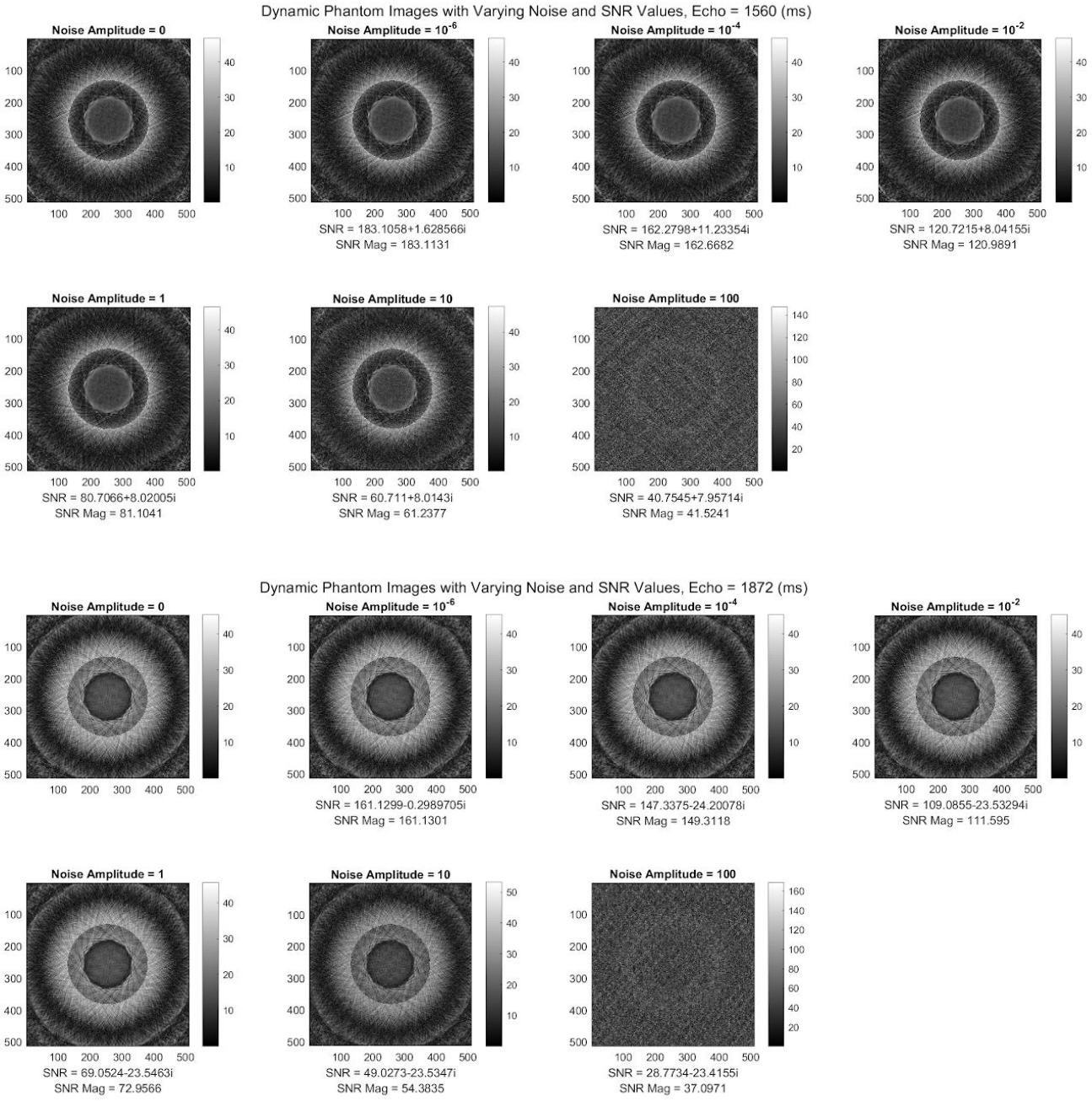

Figure V13 and V14:

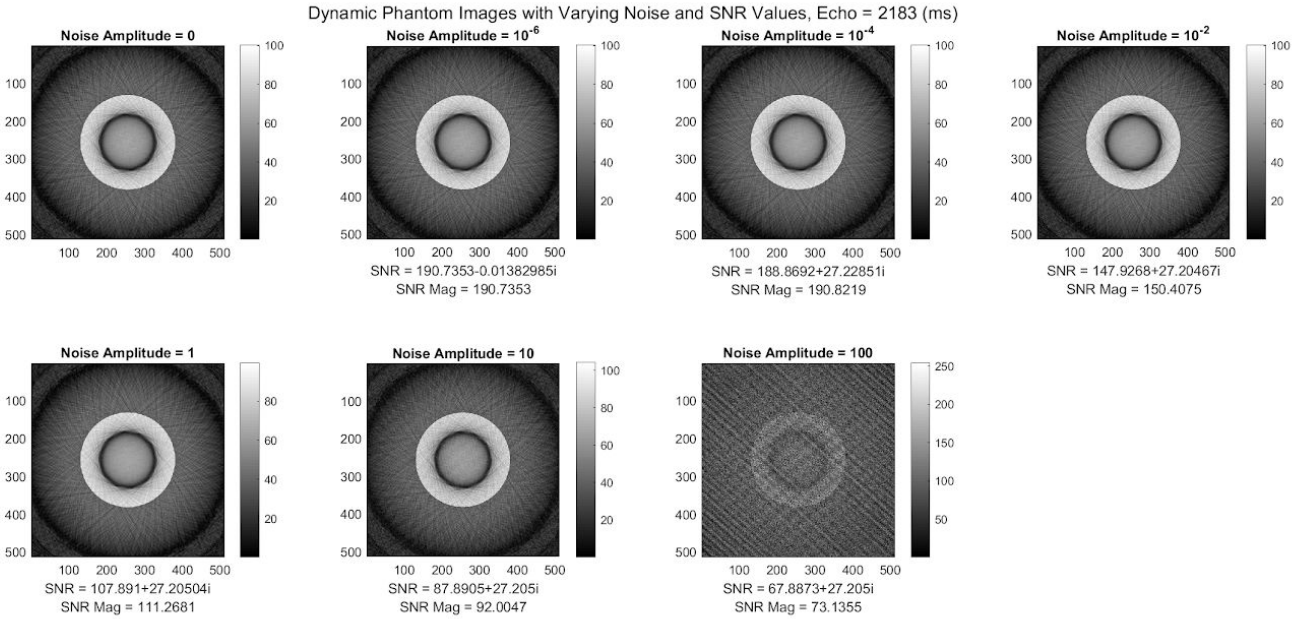

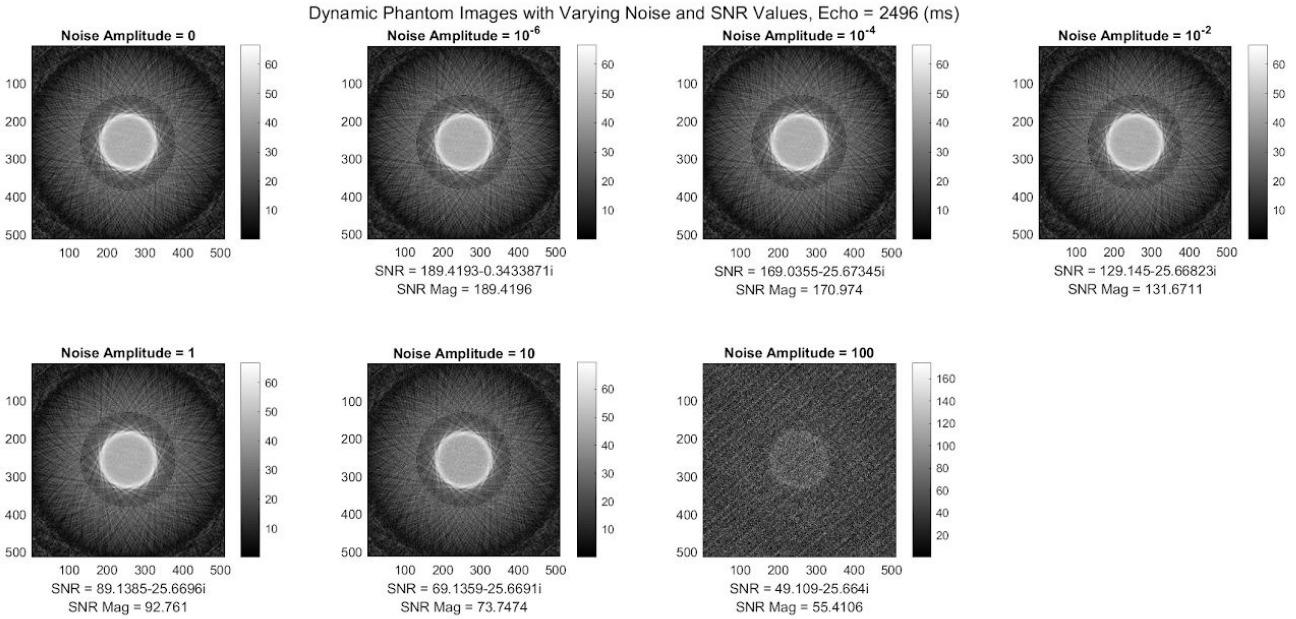

Figure V15 and V16:

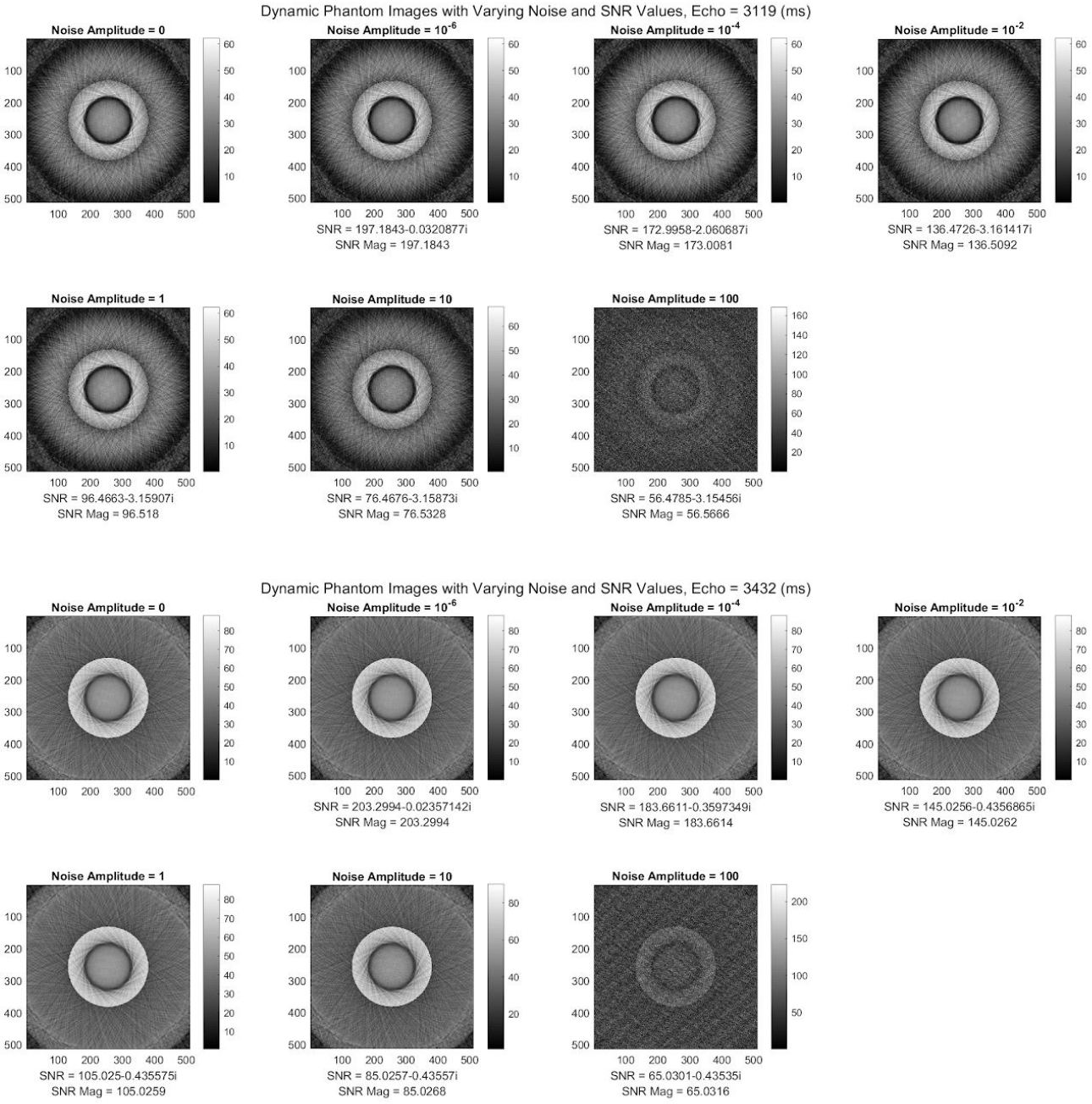

Dynamic Phantom Oscillation Images from SNR Calculation:

Figure V29 and V30:

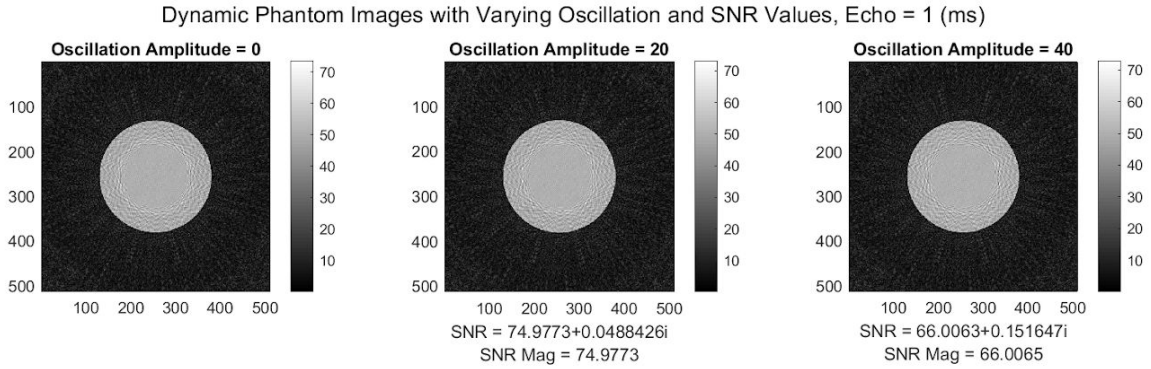

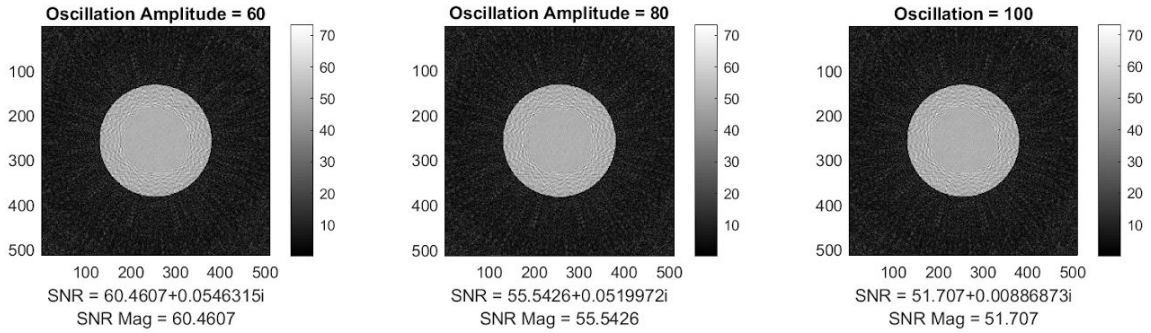

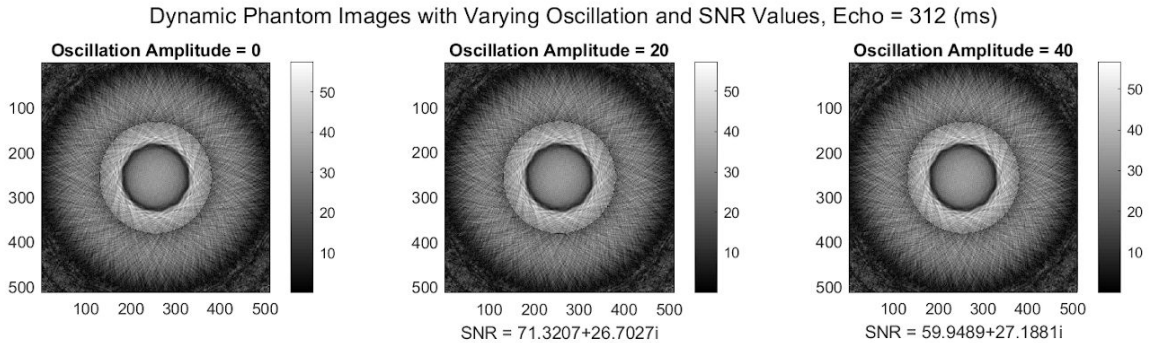

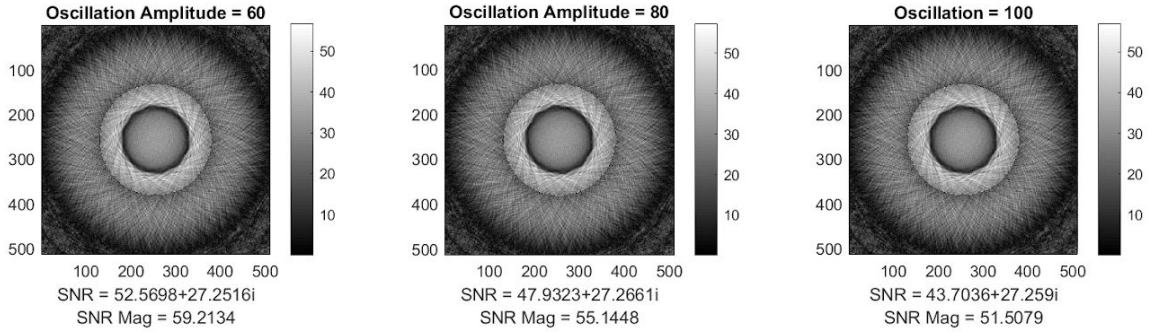

Figure V31 and V32:

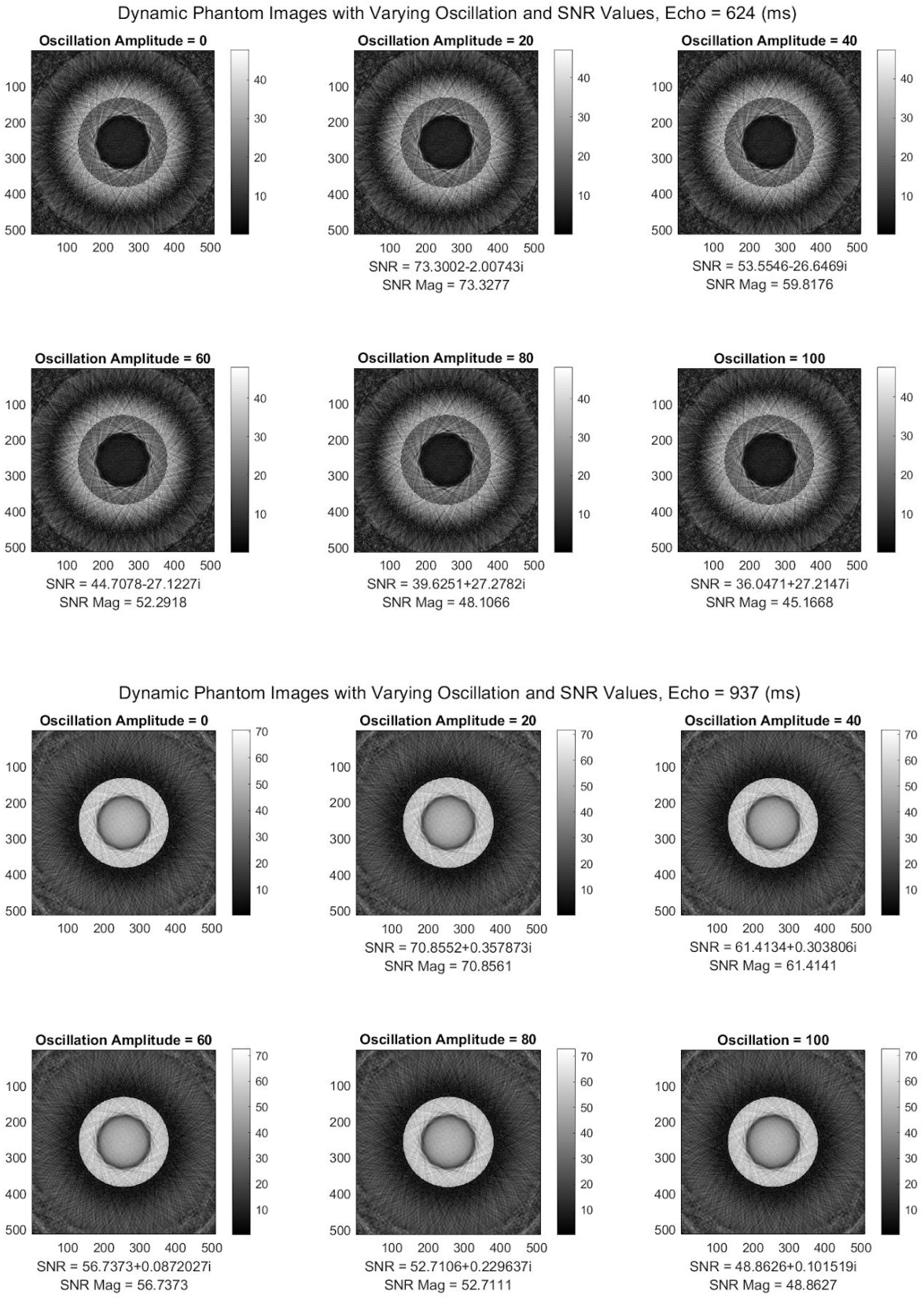

Figure V33 and V34:

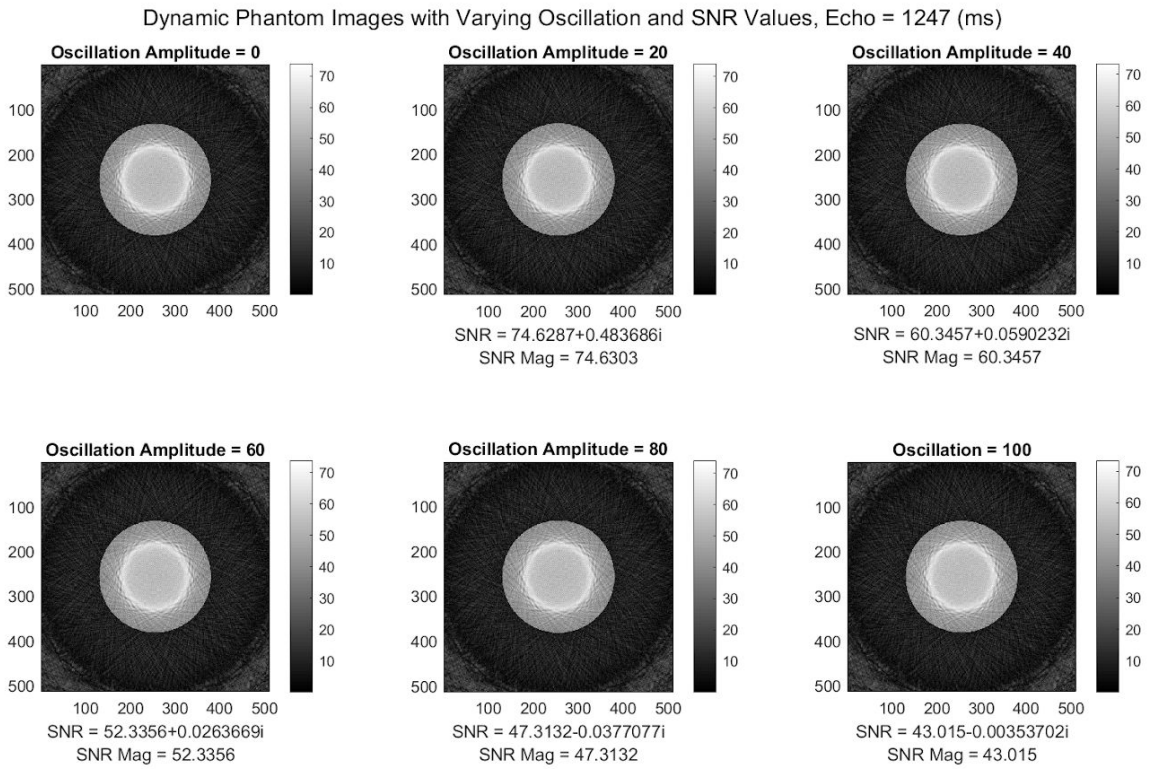

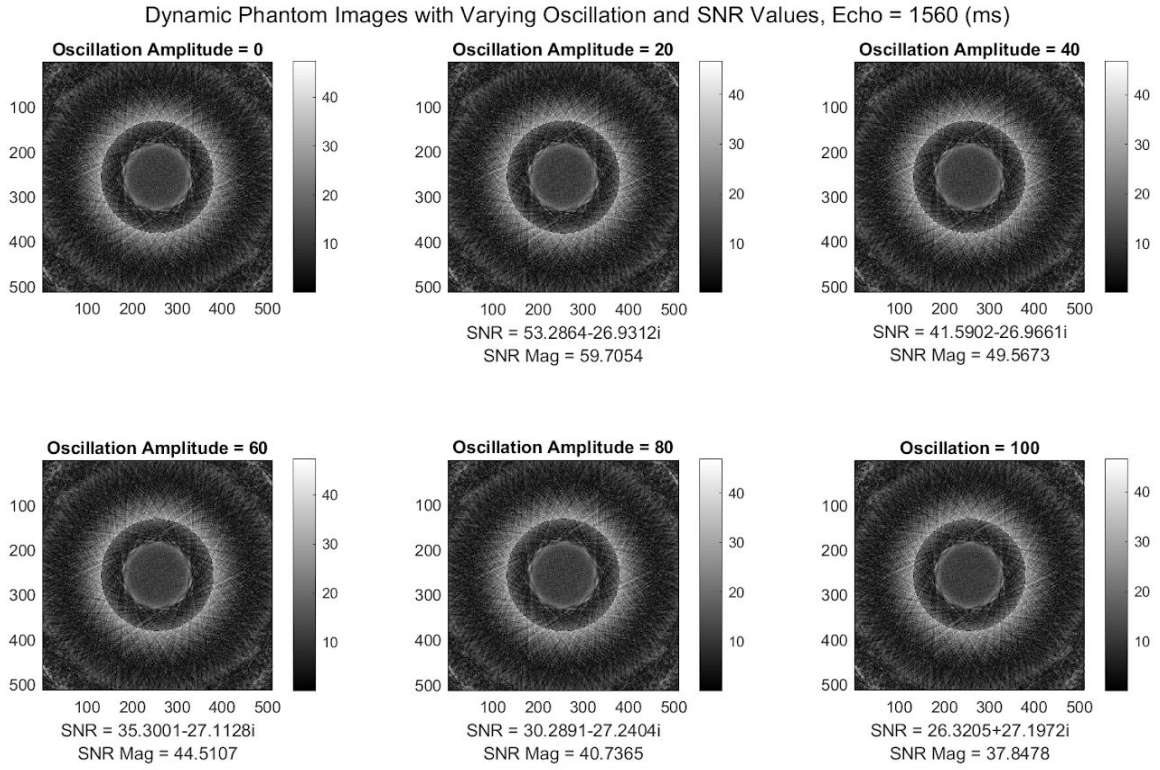

Figure V35 and V36:

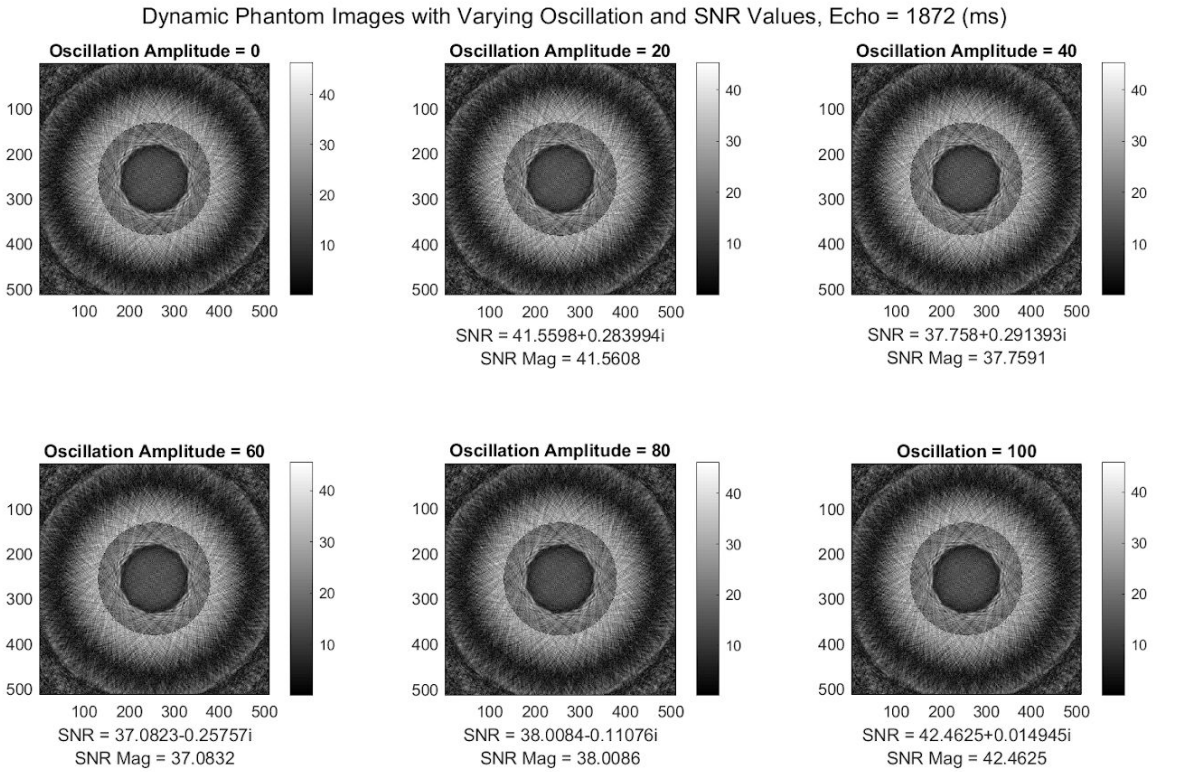

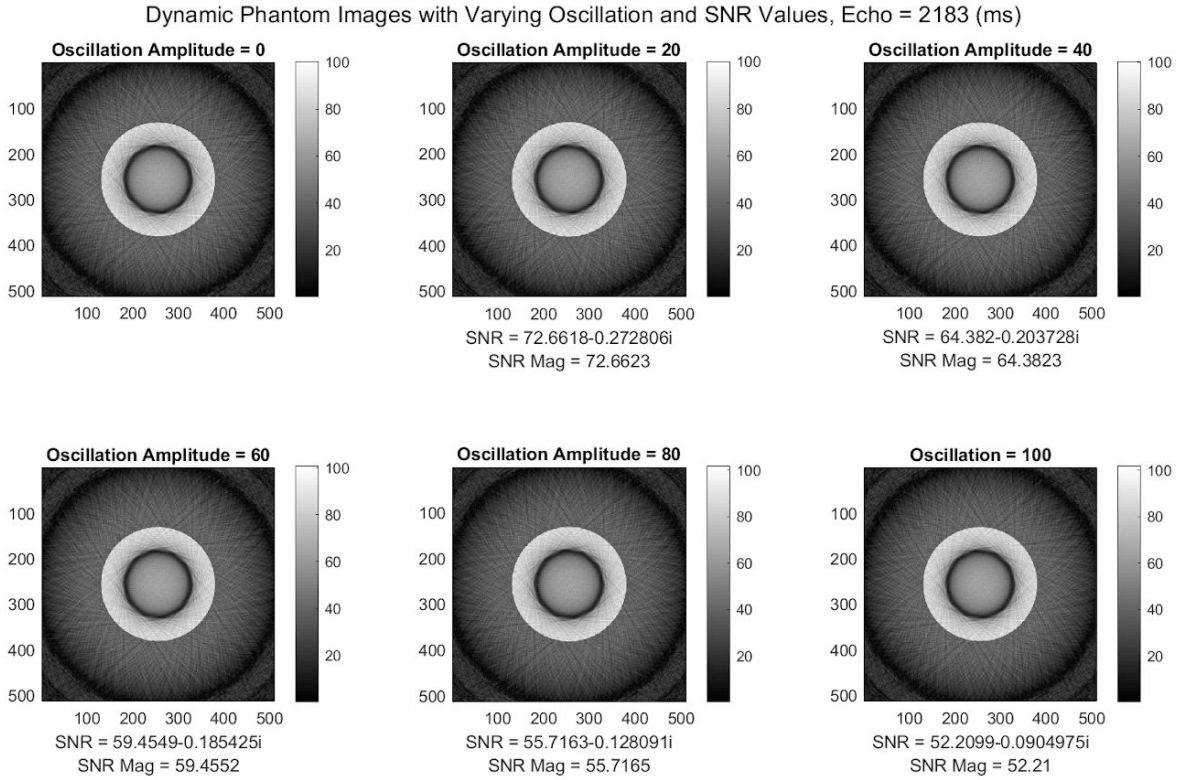

Figure V37 and V38:

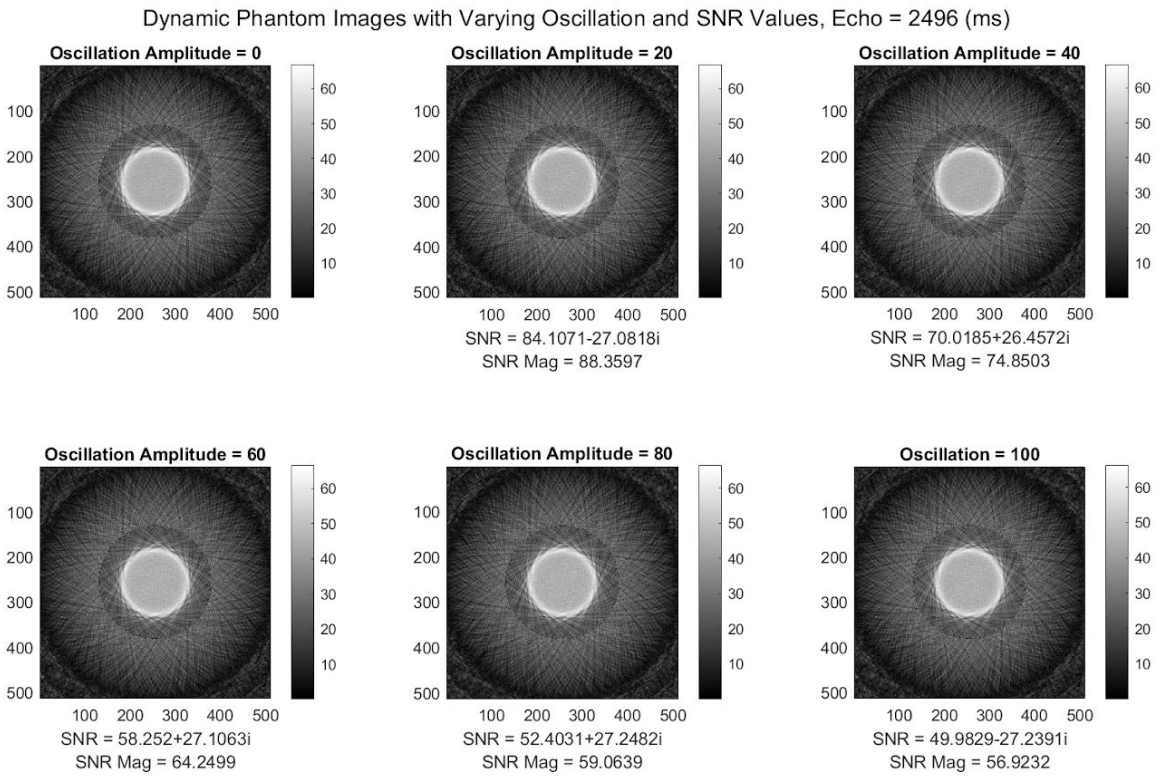

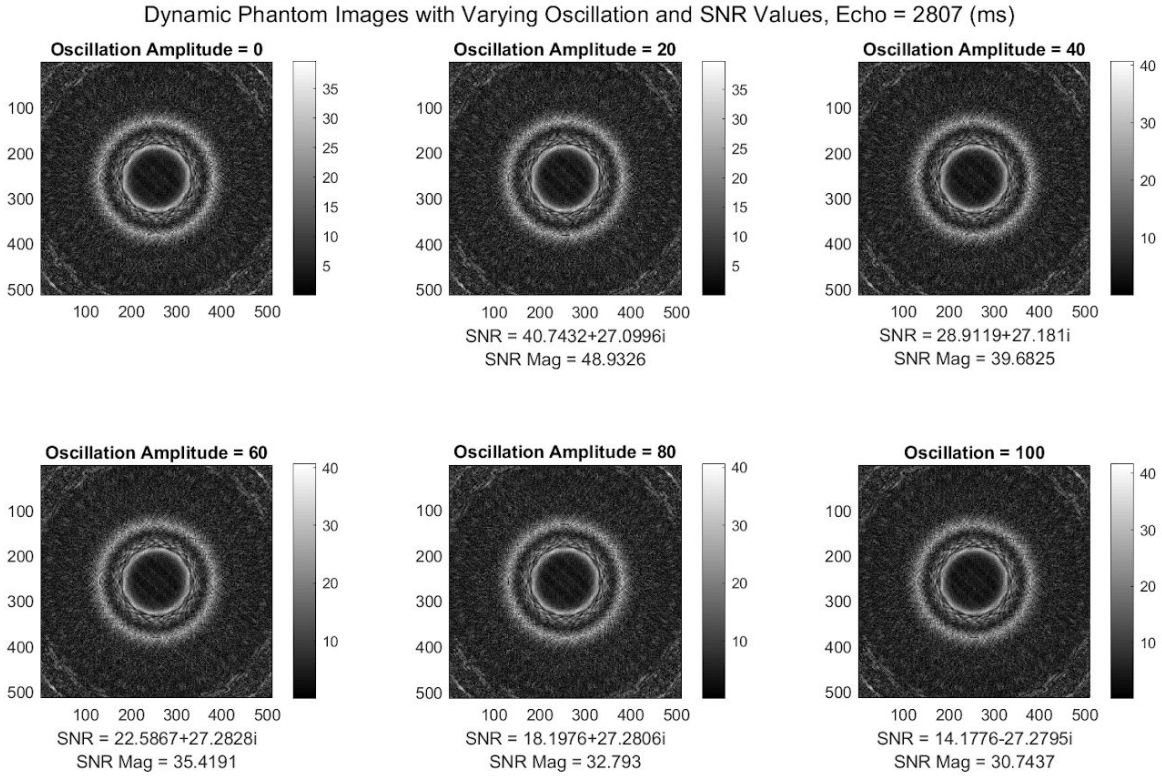

Figure V39 and V40:

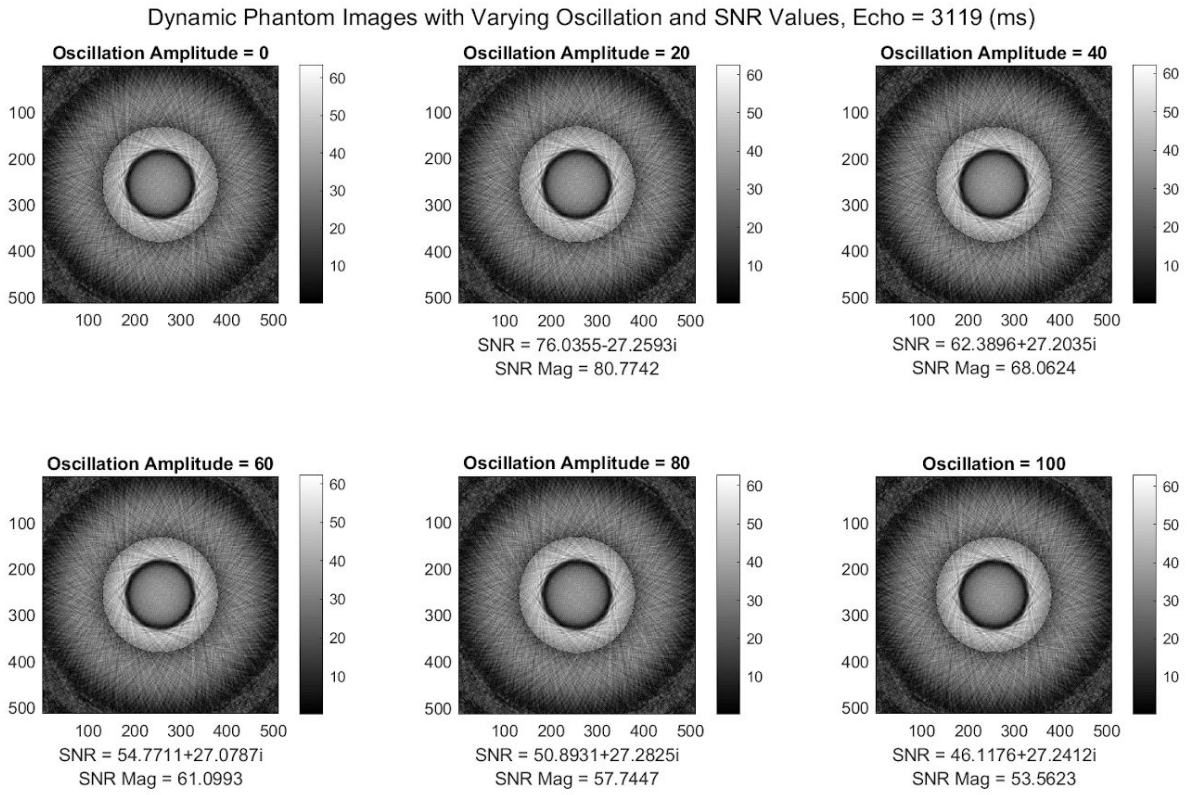

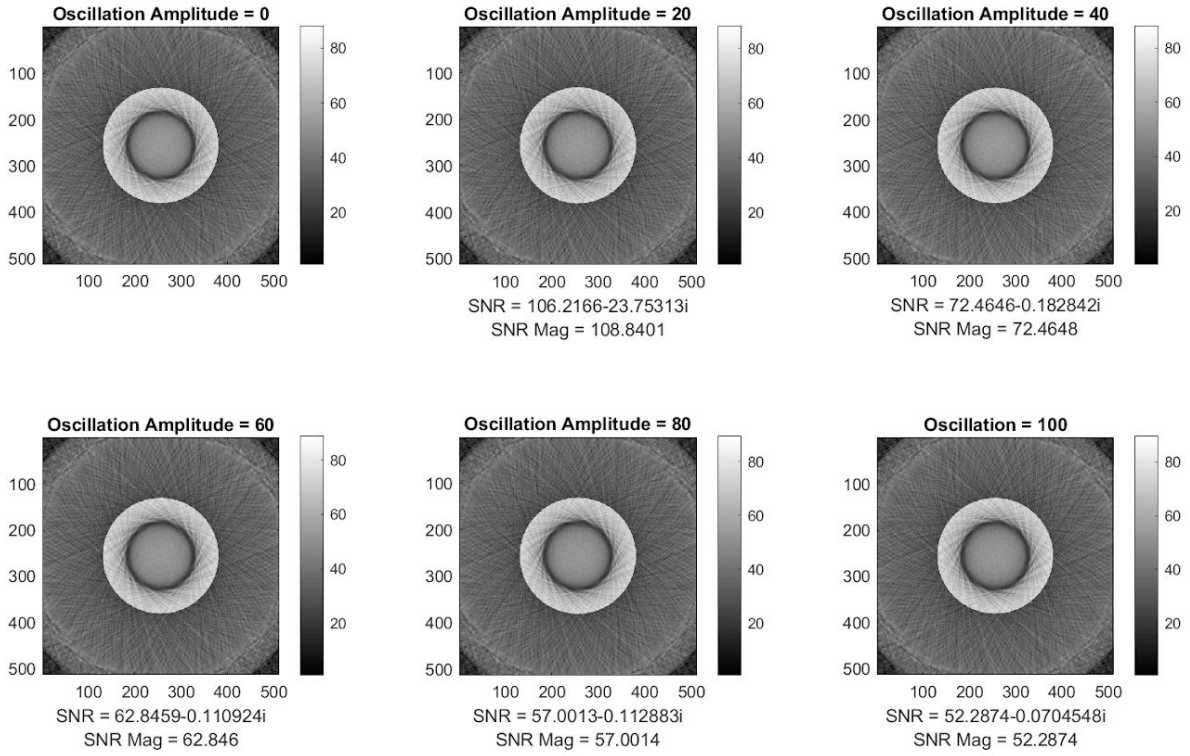

JAA Appendix:

I. Figures:

Figure 1: Off-Res Images at Positive and Negative Frequencies

A.

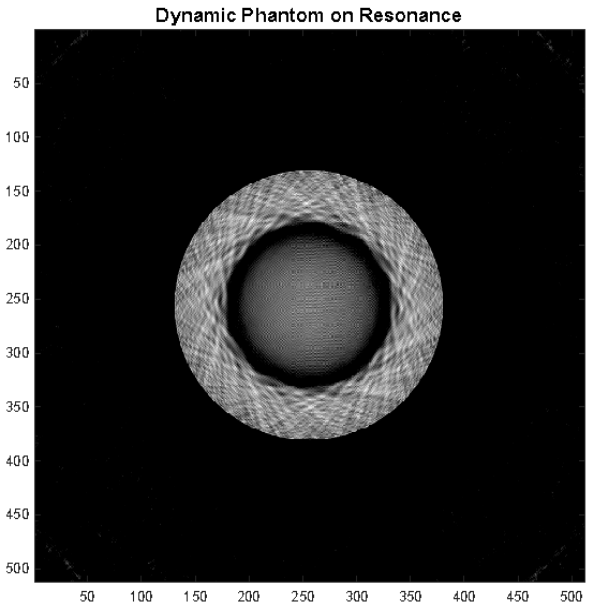

B.

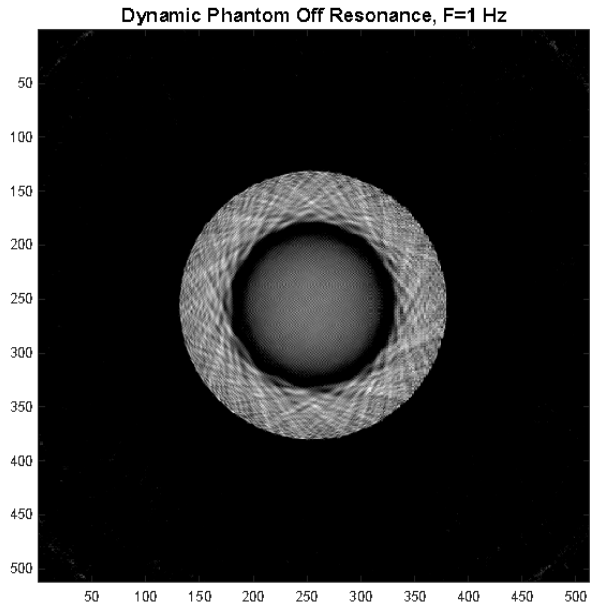

C.

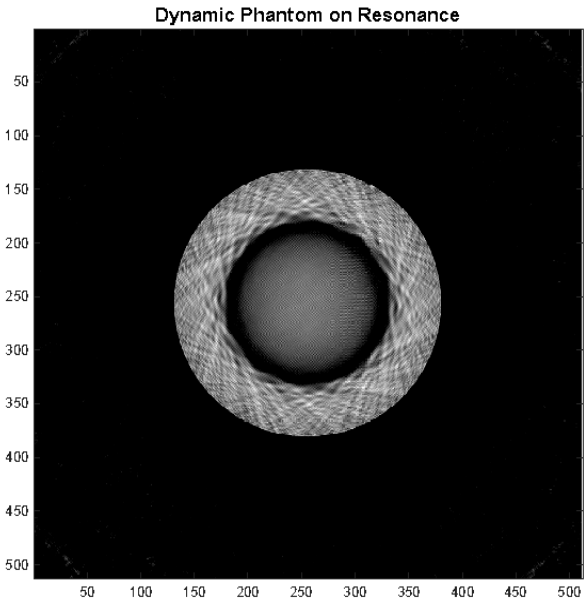

D.

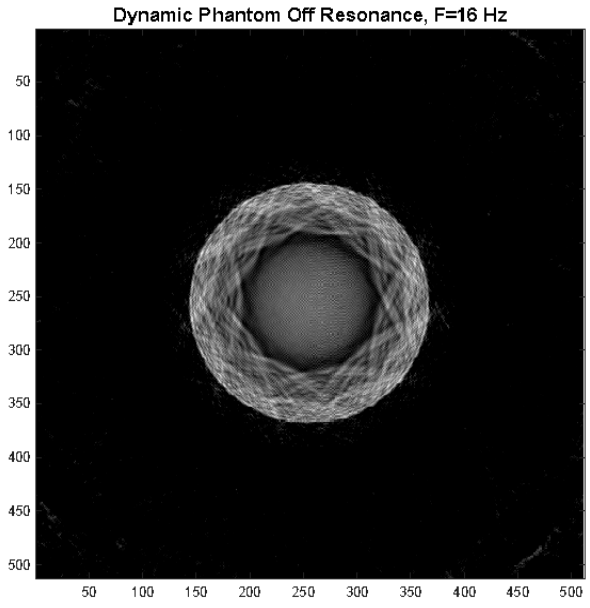

E.

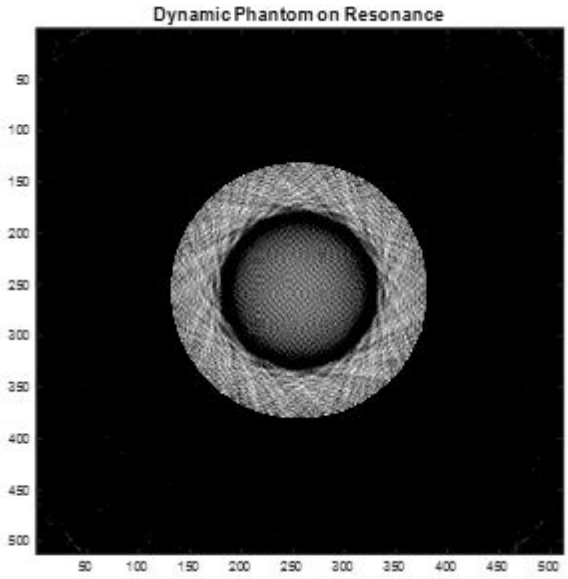
Dynamic Phantom on Resonance
50
100
150
200
250
300
350
400
450
500

F.

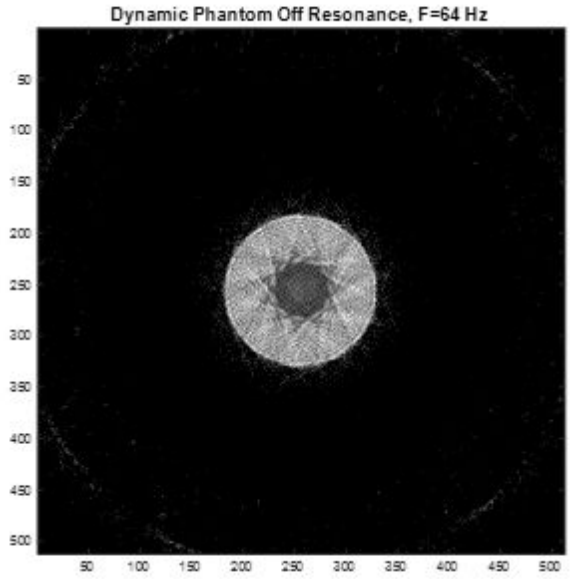
Dynamic Phantom Off Resonance, F=64 Hz
50
100
150
200
250
300
350
400
450
500

G.

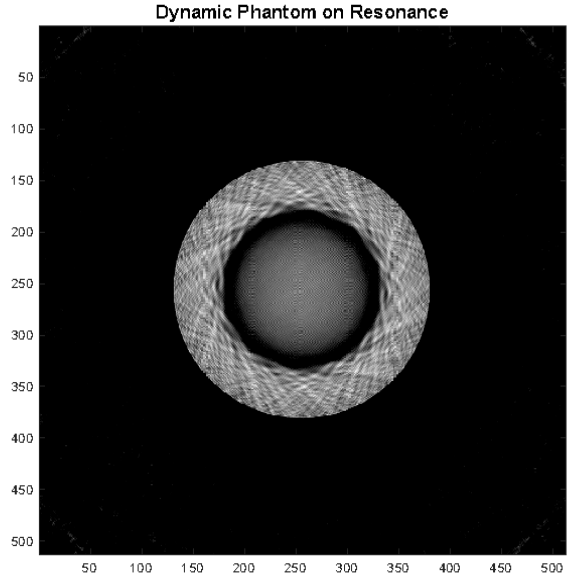
Dynamic Phantom on Resonance
50
100
150
200
250
300
350
400
450
500

H.

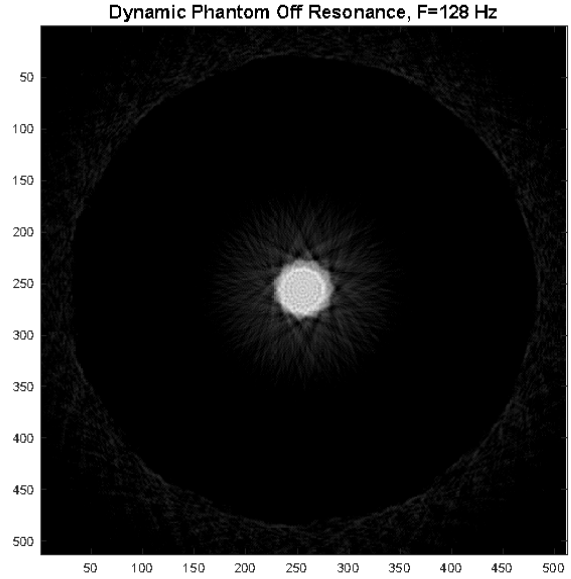
Dynamic Phantom Off Resonance, F=128 Hz
50
100
150
200
250
300
350
400
450
500

I.

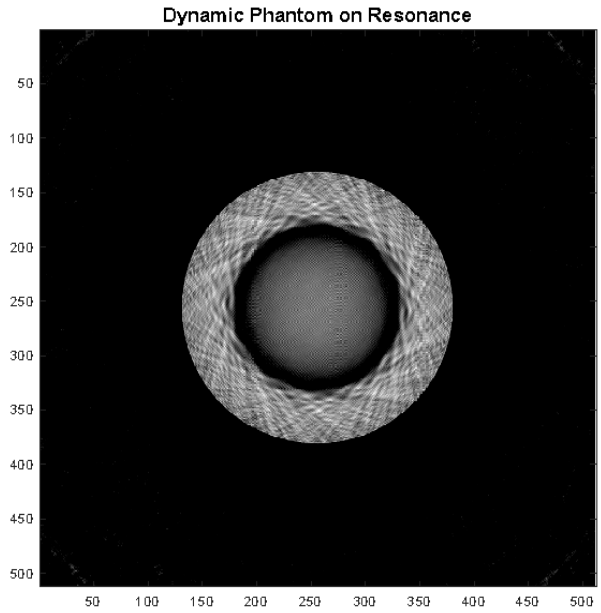
Dynamic Phantom on Resonance
50
100
150
200
250
300
350
400
450
500

J.

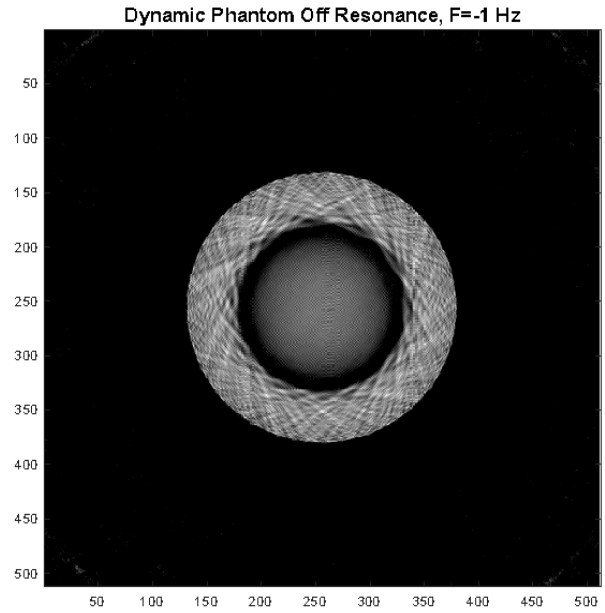
Dynamic Phantom Off Resonance, F=-1 Hz
50
100
150
200
250
300
350
400
450
500

K.

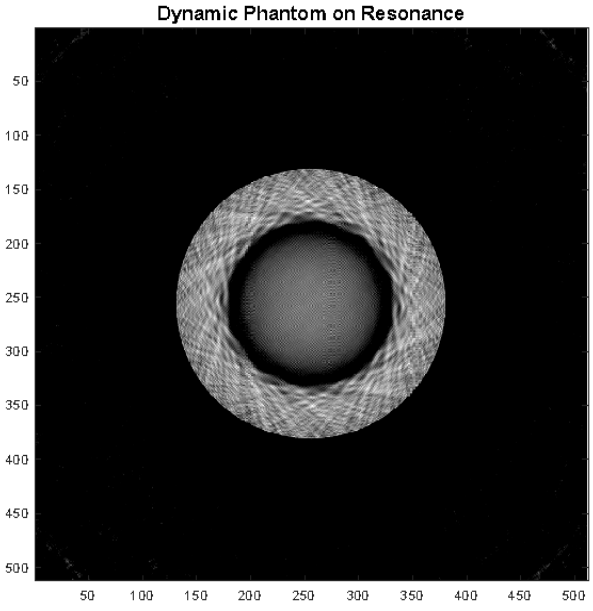
Dynamic Phantom on Resonance
50
100
150
200
250
300
350
400
450
500

L.

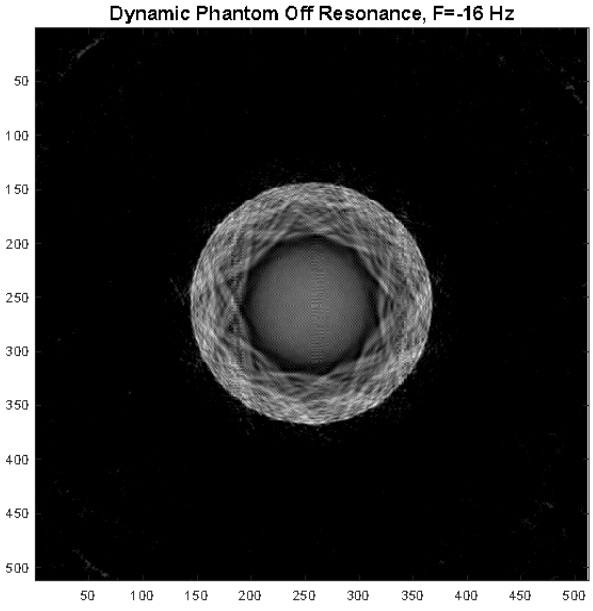
Dynamic Phantom Off Resonance, F=-16 Hz
50
100
150
200
250
300
350
400
450
500

M.

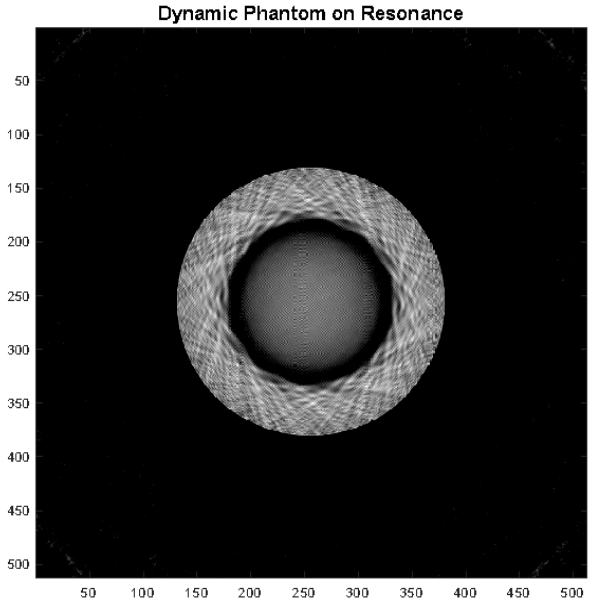
Dynamic Phantom on Resonance
50
100
150
200
250
300
350
400
450
500

N.

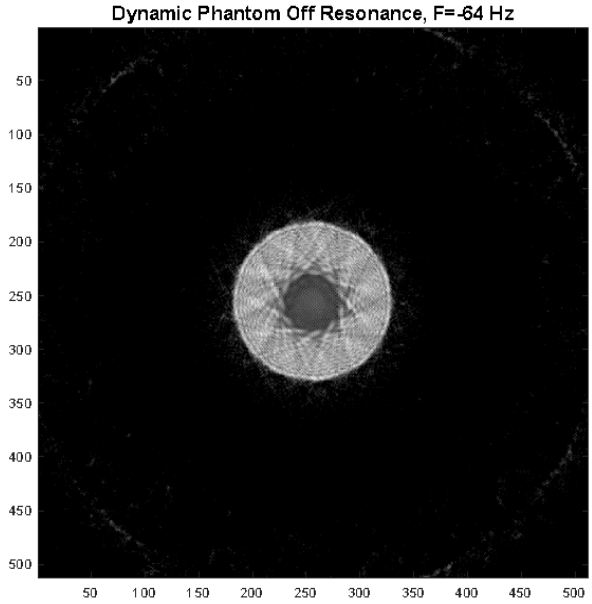
Dynamic Phantom Off Resonance, F=-64 Hz
50
100
150
200
250
300
350
400
450
500

O.

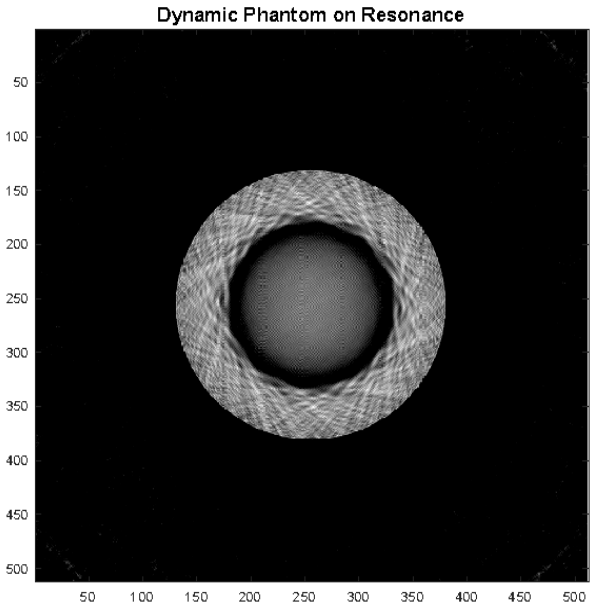
Dynamic Phantom on Resonance
50
100
150
200
250
300
350
400
450
500

P.

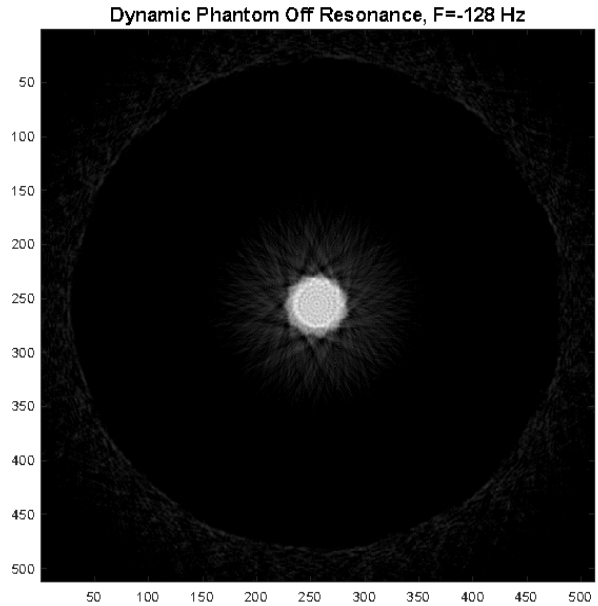
Dynamic Phantom Off Resonance, F=-128 Hz
50
100
150
200
250
300
350
400
450
500

Figure 2: Effect of Changing Number of Petals on the SNR of Off-Res Images

Off-Res Effects: 5 Petals

A. **B.**

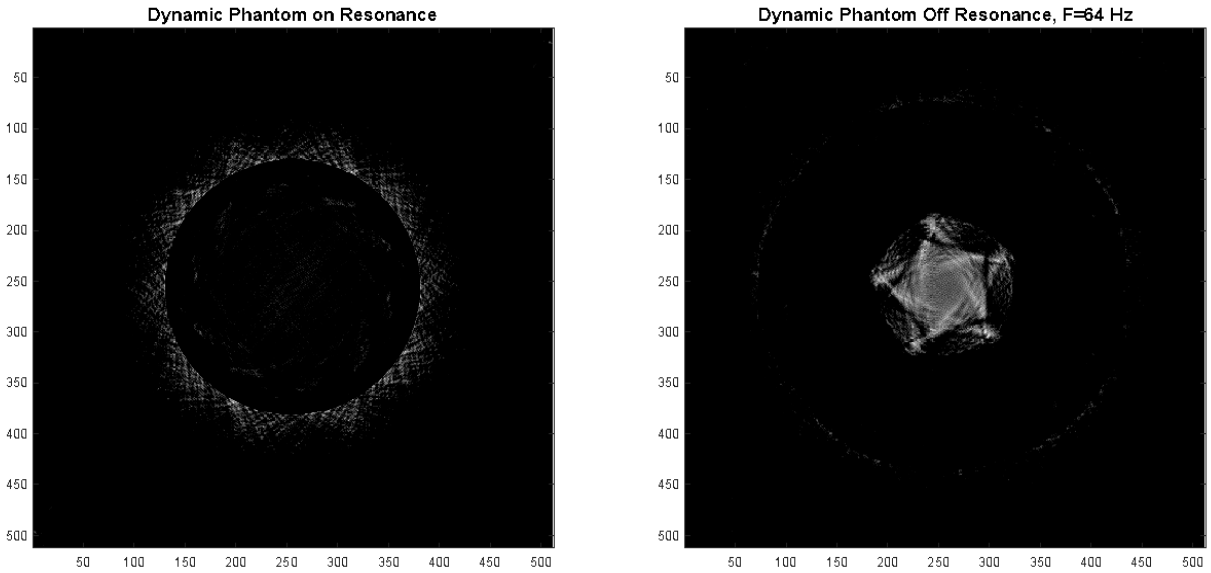

Off-Res Effects: 7 Petals

C. **D.**

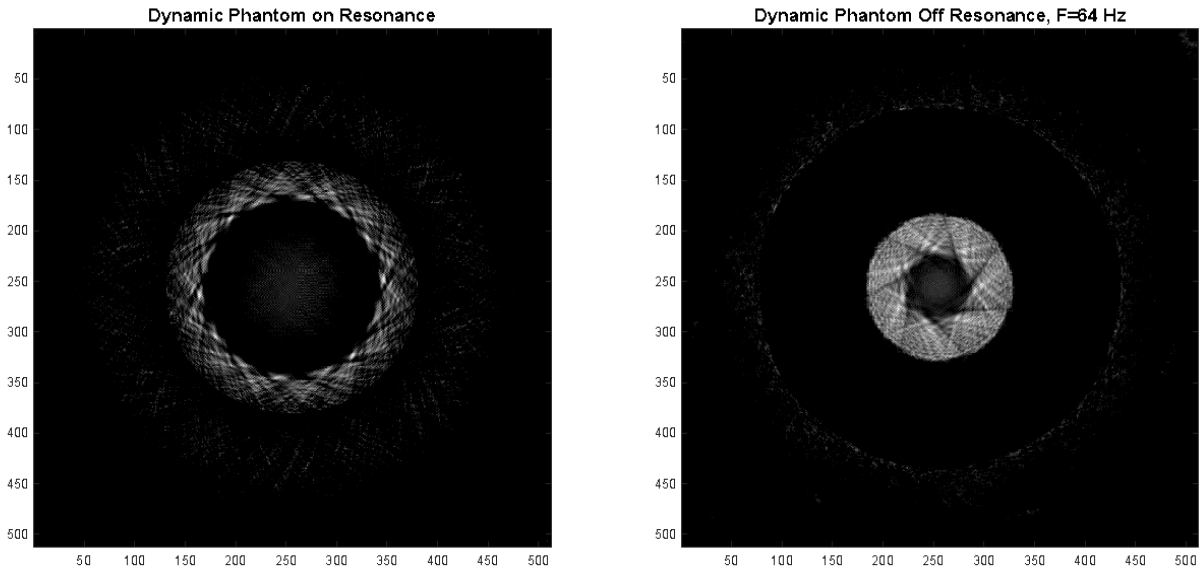

Off-Res Effects: 13 Petals

E.

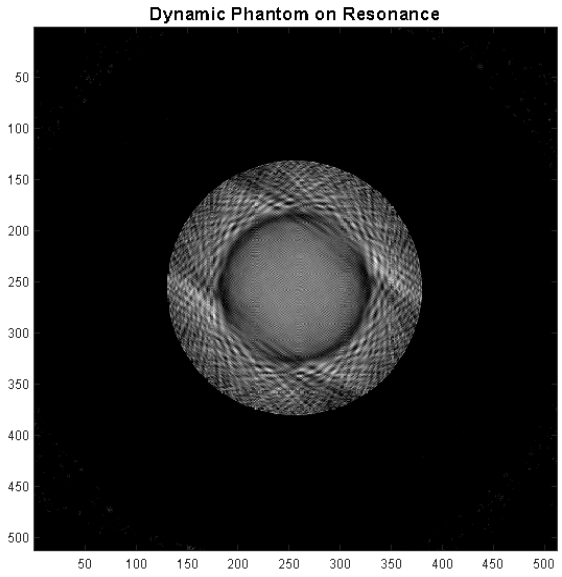

F.

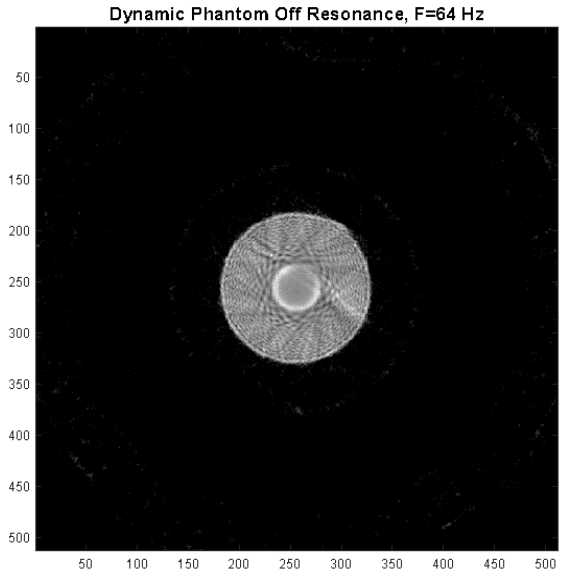

II. Tables

Table 1: Quantitative Metrics for Results Section I.

S.No	Frequency (Hz)	MSE	PSNR	R^2-Value	RMSE	NRMSE	MAPE	SSIM
1a.	1	0.032	63.127	0.983	0.178	0.098	11.30	0.491
1b.	-1	0.032	63.131	0.984	0.178	0.098	11.269	0.494
2a.	16	0.105	57.936	0.947	0.323	0.178	21.923	0.408
2b.	-16	0.105	57.933	0.947	0.323	0.178	21.809	0.415
3a.	64	0.613	50.257	0.689	0.783	0.429	59.836	0.221
3b.	-64	0.611	50.269	0.69	60.493	0.9	59.701	0.217
4a.	128	0.83	48.942	0.579	0.911	0.5	44.019	0.163
4b.	-128	0.83	48.943	0.579	0.911	0.498	44.041	0.166

Table 2: Effect of Changing Number of Petals on SNR of Off-Res Image

S.No.	Number of Petals	Resonance Condition	Peak Frequency (Off-Res)	SNR
1.	5	On-Resonance	-	175.01
		Off-Resonance	64Hz	179.05
2.	7	On-Resonance	-	202.54
		Off-Resonance	64Hz	201.08
3.	13	On-Resonance	-	195.7
		Off-Resonance	64Hz	192.12

III. Supplementary Material

Quantitative Metrics for Image Quality:

i. MSE (Mean Squared Error): The MSE is an estimator that measures the average of the squared differences between the actual and predicted values. The lower the MSE, the better the agreement between predicted and actual images.

$$MSE = mean(Predicted - Actual)^2 \quad -(3)$$

ii. PSNR (Peak Signal to Noise Ratio): The PSNR measures the maximum power of a signal compared to the amount of noise corrupting the image. The higher the PSNR, the better the correlation between the predicted and actual images.

$$PSNR = 10\ log_{10} \frac{Max\ Pixel\ Value^2}{MSE} \quad -(4)$$

iii. R^2-Value: The R-Squared Value measures the proportion of variance for a dependent variable explained by an independent variable in a regression model. The range of R-squared is from 0 to 1, with 1 implying 100% linearity.

$$R^2 = 1 - \frac{Sum\ of\ Squares\ of\ Residuals}{Sum\ of\ Total\ Squares} \quad -(5)$$

iv. RMSE (Root Mean Squared Error): The RMSE measures the quadratic mean of the differences between predicted and actual values. Similar to MSE, low values of RMSE correlate with better agreement of the predicted and actual images.

$$RMSE = \sqrt{\sum_{i=1}^{n} \frac{(Predicted - Actual)^2}{n}} \quad -(6)$$

v. NRMSE (Normalized Root Mean Squared Error): The NRMSE is calculated by normalizing the RMSE and guarantees a one-to-one comparison between the two images. As expected, a lower NRMSE implies better correlation.

$$NRMSE = \frac{RMSE}{Max\ Observed\ Value - Min\ Observed\ Value} \quad -(7)$$

vi. MAPE (Mean Absolute Percentage Error): The MAPE is a common loss function used to solve regression problems calculated as the average of the absolute percentage differences between the actual and predicted values. Like most error metrics, a smaller error relates to a higher correlation between the predicted and actual image.

$$MAPE = \frac{100}{n} \sum_{i=1}^{n} \left| \frac{Actual - Predicted}{Actual} \right| \quad -(8)$$

vii. SSIM (Structural Similarity Index): The SSIM measures the degree of similarity between two images using more perceptual phenomenon. If two images are perceived as similar by the human eye, there is a good chance that they will have a high SSIM value. The higher the SSIM, the better agreement between the predicted and actual images.

$$SSIM(x,y) = \frac{(2\mu_x\mu_y + C_1)(2\sigma_{xy} + C_2)}{(\mu_x^2 + \mu_y^2 + C_1)(\sigma_x^2 + \sigma_y^2 + C_2)} \quad -(9)$$

$\mu_x,\ \mu_y$ = *Mean of Predicted and Actual Image*

$\sigma_x,\ \sigma_y, \sigma_{xy}$ = *Variance of Predicted, Actual & Predicted and Actual Image*

$C_1,\ C_2$ = *Covariance of Predicted and Actual Image*